RSC Advances

PAPER

View Article Online
View Journal | View Issue

Cite this: *RSC Adv.*, 2025, **15**, 40129

Prognosis of simplified metal and organic sites resembling a quasi-MOF structure for hydrogen storage: investigation and insight

Ruiqi Lyu, *[a] Xiangya Xu,[a] Yi Man,[b] Yu Bai,[b] Wei Li[a] and Dongbing Liu [a]

Hydrogen energy plays an important strategic role as a sustainable and clean energy source for the future, and the use and efficient design of hydrogen storage and transportation materials are essential. Exploration into the usage and efficient design of hydrogen energy storage and transportation materials is necessary. However, a state of confusion and uncertainty exists regarding the similar operational mechanisms and details of hydrogen storage materials. This article focuses on the study of Zr-, Co-, In-, and Cu-based gas adsorption materials represented by metal organic framework (MOF)-derived structures. In this work, the basic unit planning and configuration design of metal coordination were analyzed and compared separately; the summarized working mode and rules of organic linking agents, represented by benzene-1,4-dicarboxylic acid (BDC) and its longitudinal chain derivatives, were concluded; based on experimental references, the adsorption relationship of samples under non adiabatic conditions was processed and evaluated, and the dynamic evolution process of sample gas adsorption was elucidated. Through the deployment of specific functions and non-adiabatic environment orchestration, we found that both the structural design and samples met the expected actual values, and some structural samples exceeded the theoretical level of the normal UIO-66 and MOF-74 series. This work analyzes and advocates for a potential benign hydrogen adsorption scheme using a MOF morphology, provides potential adsorption materials that can improve environmental tolerance, and reveals their adsorption response laws. Ultimately and fortunately, these materials could become strong competitors in the field of hydrogen storage functional materials.

Received 18th August 2025
Accepted 8th October 2025

DOI: 10.1039/d5ra06111c

rsc.li/rsc-advances

Introduction

The development of materials with effective storage has always been a controversy in the field of metal–organic framework (MOF) materials, as the factors that determine their storage values have been explained by a variety of theories in microporous material field.[1–4] Hydrogen uptake capacity has been identified as an advantageous feature in microporous materials. Commercial MOFs such as MOF-5 [5,6] zeolitic imidazolate frameworks (ZIF-8) [7,8] and the Hong Kong University of Technology (HKUST) series[9,10] have shown improved performance due to their tunable porosity and expandable connectivity. However, their practical application is hindered by their theoretical absorption limits under conditions of 500–600 °C (decomposition temperature) and 20–100 bar (allowable pressure) [11–13] which remain a persistent and significant challenge for conventional organic porous materials. In addition, their geometric conformation and topological character are another concern for researchers due to their morphologies.[14–18] As the main basic elements that determine the storage and transportation are the metal coordination (MC) and organic linker (OL), there are various intriguing aspects in the structure of MOFs, such as ordered/disordered resetting,[19] hierarchical transition,[20] symmetry designs derived from the metal particle space group[21] and multicomponent conjugated growth.[22] In these designs, the MC and OL can induce characteristic structures with precise pores and channels, enabling them to become MOF composition systems with periodic stacking.

Controlled modulation of the MCs and OLs is essential for engineering tunable open sites to enable precise customization of diverse structural configurations and physicochemical properties.[23,24] In general, most metal–organic frameworks (MOFs) can be functionalized using Lewis or Brønsted acid sites associated with their metal clusters. To tailor the confined chemical environment, post-synthetic modification strategies, such as introducing ordered surface functionalization around the cages, have been employed during the early stages of MOF crystallization. Zhang *et al.* synthesized Co and Ni nanosheets *via* a bottom-up liquid–liquid interfacial coordination

[a]*Department of Catalytic Science, SINOPEC Beijing Research Institute of Chemical Industry, Co., Ltd, Beijing, 10013, P. R. China. E-mail: Lrainbowchaser77@163.com; xuxy.bjhy@sinopec.com; liwei.bjhy@sinopec.com; liudb.bjhy@sinopec.com*

[b]*Division of Analysis, SINOPEC Beijing Research Institute of Chemical Industry, Co., Ltd, Beijing, 10013, P. R. China. E-mail: many.bjhy@sinopec.com; baiy40585.bjhy@sinopec.com*

polymerization approach.[25] This method facilitates the formation of ordered nanochannels and layered architectures, which not only offer abundant metal active sites within the flexible coordination nanosheets, but also significantly enhance hydrogen adsorption efficiency. Gibbons *et al.* enhanced the structural stability of MOFs under mild conditions and improved their tolerance for hydrogen absorption by symmetrically modifying OL and performing cyanoalkylation on imine skeletons in prototype porous frameworks such as UiO-66 (University of Oslo) and MOF-74.[26] These methods contribute to various coordination strategies and joint modifications to enhance the hydrogen adsorption capacity of MOFs, and integrating MC into open sites *via* ion coordination has proven effective in pore engineering. Through exploring the characteristic distribution of metal sites in MOFs and extending the main-chain length of OLs to fine-tune pore apertures, these strategies have successfully enabled the formation of repetitive heterogeneous pore assemblies without relying on highly branched architectures.

Recently, quasi-MOFs have emerged as a promising strategy to overcome the symmetry constraints imposed by the hollow pore structures of conventional MOFs.[5,27–31] They not only improve adsorption efficiency but also allow fine-tuning of geometric morphology, which is a feature that is often underoptimized in traditional MOF systems. Moreover, unlike the fully coordinated metal clusters in pristine MOFs, quasi-MOFs possess sparse yet highly accessible vacancy sites. These can effectively convert external vacancies into specific target vacancies, resulting in significant Faraday efficiency and selectivity,[32–34] which can effectively weaken the steric hindrance in MOFs. Kampouri *et al.* successfully designed a quasi MOF structure with coordination vacancies (X-UIO-EDA), which has a hydrogen capture capacity of 0.44 mmol g^{-1} at a concentration of 400 ppm and humid air conditions. Compared with traditional UIO-66, the adsorption performance brought by its structure is improved by 6.5%.[35] By leveraging multi-coordinate structures simulated *via* molecular dynamics (MD),[36,37] intermediate vacancies can be incorporated into quasi-MOF frameworks. Listyarini *et al.* conducted MD simulations on a quasi-MOF structure formed by controlling vacancies in MOF-5 and obtained a highly consistent structure with the experimental results of the guest@host system. They inferred that H_2 and CO_2 have a high degree of dissociation in their quasi-MOF structure.[38] These vacancies play a critical role in the formation of cage-like composite architectures. Importantly, the use of MD for quasi-MOFs has achieved high adsorption performance without the need for prolonged reaction times, large-scale simulations involving active atoms, or computationally demanding quantum mechanical calculations.[39–41] Given these advantages, precise adjustment of the MCs and control of the OL chain length have become crucial for quasi-MOF systems, and further analysis and exploration of their unknown properties are necessary.

In this study, hydrogen absorption in metal–organic frameworks (MOFs) was investigated by integrating coordination methods and various OL decorations. The adsorption behavior and potential mechanisms were evaluated over an extended temperature range. The quasi-MOF architectures were constructed using symmetric secondary noble metal clusters (comprising Zr, Co, Cu, and In) with tailored coordination geometries. Based on this, we developed a coordinated coarse-grained (CG) layout pattern to evaluate the synergistic existence of effective bonding relationships and topological spaces within coordination numbers in the studied structures. The experimental absorption range and theoretically optimized storage capacity were dynamically analyzed by observing MOF samples under experimental conditions and using simulated (MD) results. The increased flexibility of the MOF framework in the In and Co samples resulted in the expansion of the porous space, significantly improving the absorption capacity of the material. In order to evaluate gas adsorption performance and predict hydrogen absorption trends, we systematically studied longitudinal OL components containing BDC, BPDC ([1,1′-biphenyl]-4,4′-dicarboxylic acid), and TPDC ([1,1 : 4′,1′-triphenyl]-4,4′-dicarboxylic acid) linkers and investigated the effect of their structural modification on hydrogen adsorption. These topologically engineered MOF candidates exhibit excellent structural loading and highly competitive adsorption capabilities.

Results and discussion

The structural relationships in MOFs are a key factor influencing their adsorption performance. Based on the critical role of Coulomb interactions in analyzing the missing coordination atoms in MOF structures,[42,43] we conducted detailed structural characterization and Coulomb interaction analysis of the synthesized samples and determined the corresponding conformational relationships, as shown in Fig. 1. Although some specific alloys or metal dimers exhibit many photonic band gaps, their parallel polyhedral distributions may adopt lower energy configurations, such as the three-coordinate or four-coordinate structures shown in Fig. 1(a)–(d). Theoretical analysis shows that energy-stable atomic rearrangement occurs through the coordinated flipping of occupied states and discrete atomic displacement,[44,45] and that these structures maintain the global minimum energy of the system. By using the established interatomic potential (Coulomb potential) for short-range computational simulations, substantial differences in electronic structures between the intermetallic compounds were revealed. Our results indicate that among the tested samples, the indium-based sample exhibits the highest coulomb interaction, while the cobalt-based sample exhibits the lowest (Fig. 1(e)). This trend, coupled with their coordination numbers, indicates the stability of the structure and the availability of corresponding coordinatively unsaturated sites, especially for the indium samples exhibiting higher coordination numbers. The unique valence electron configuration of the constituent metal dominates the interaction between the MC and OL, and conforms to the Hume-Rothery stability rule.[46,47]

In order to reveal the above, we used an OPLS-AA force field to perform structural equilibrium relaxation of the material structure with a box size of 6 × 6 × 6 and a time step of 2 fs. Temperature control was conducted using the Nosé–Hoover

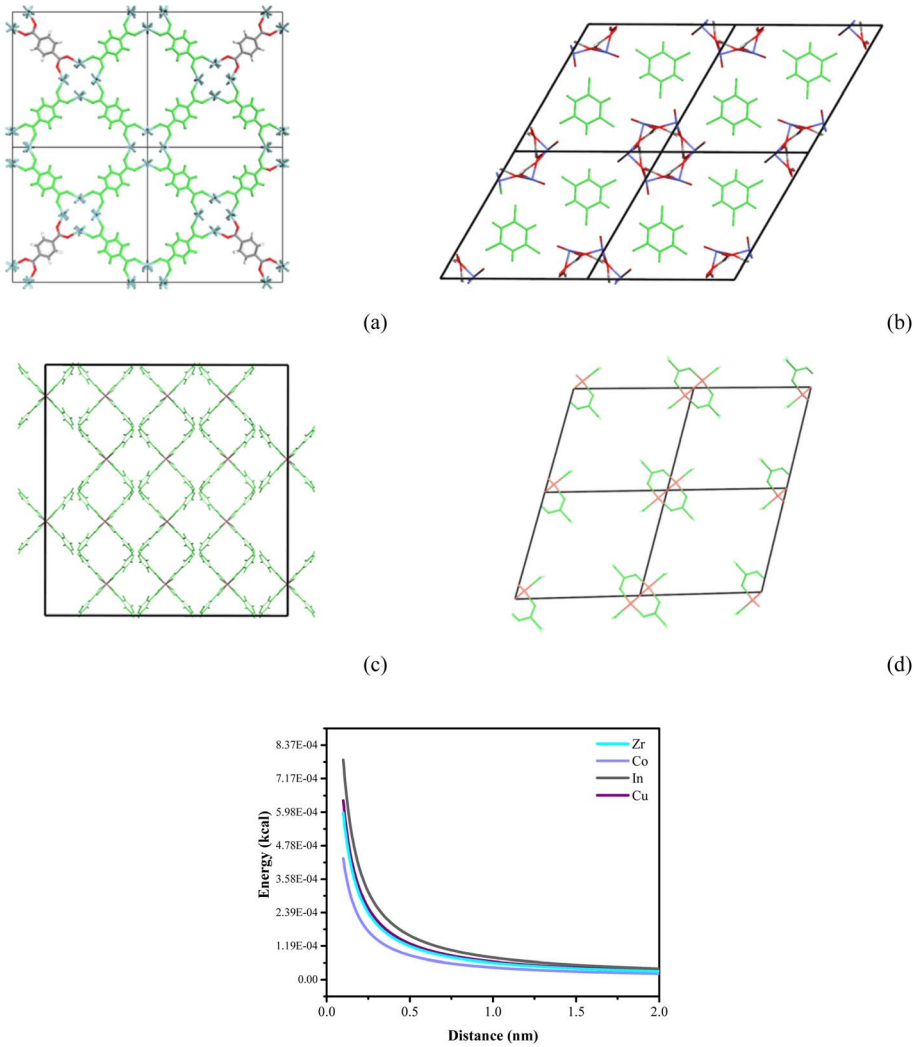

Fig. 1 Structural conformation (a)–(d) and coulomb interaction (e) within the unit crystal (simulation box). The OLs are shown in green; in the other parts, Zr is shown in cyan (a), Co in blue (b), In in silver-gray (c), and Cu in orange (d). The Coulomb interaction curves (e) are shown in cyan (Zr), clear blue (Co), silver grey (In), and dark purple (Cu), respectively.

method, and pressure control was carried out using the Berendsen barostat. The structural stability of the material was verified through a 10 ps thermal equilibrium. In addition, we also introduced long-range electrostatic interactions (Coulomb treatment) to ensure the stability of the truncation distance of the structural samples. Under Kornberg fitting,[48] the 4-coordinate systems for zirconium and copper offer a cost-effective precision that is superior to both the 6- and 2-coordinate systems. The process of growing the simulation boxes introduced structural defects after particles were implanted into the isohedral symmetry structure. Moreover, defect free locating, macroscopic grains and non-equilibrium relaxation emerged in binary, ternary, quaternary systems with conventional mobilized shaping techniques. As shown in Fig. 2 and Table 1, we provided the molecular dynamic simulation for effective particle interaction with a stimulus of the mixing pair potential (MPP) with 2 traps. After Lorentzo oscillation,[49] the pair potential thus mimics the atomic interaction of the MC and OL systems, and combines a short-range repulsion with a damping oscillating function $F(r)$ which specified a distance factor x damping factors k, average interactive distance r and preposed coefficient σ. Along with these quasi crystalline samples being included in our oscillation function, oscillating potential style, converging repulsing potential stlye, dividing and non dividing potential style were attended to during the function module. Our two captured MPPs are in corresponding states of gravitational and thermal disorder, which means that these simulated samples can spontaneously aggregate with hydrogen molecules under supercooled conditions.

$$x(r) = -ke^{r} \tag{1}$$

$$F(r) = k\frac{\mathrm{d}^2x}{\mathrm{d}r^2} + k\sigma\frac{\mathrm{d}x}{\mathrm{d}r} + k\sigma^2 r \tag{2}$$

As the interaction contact can be switched by means of electron transition,[15,50] a coulomb blockade was induced by

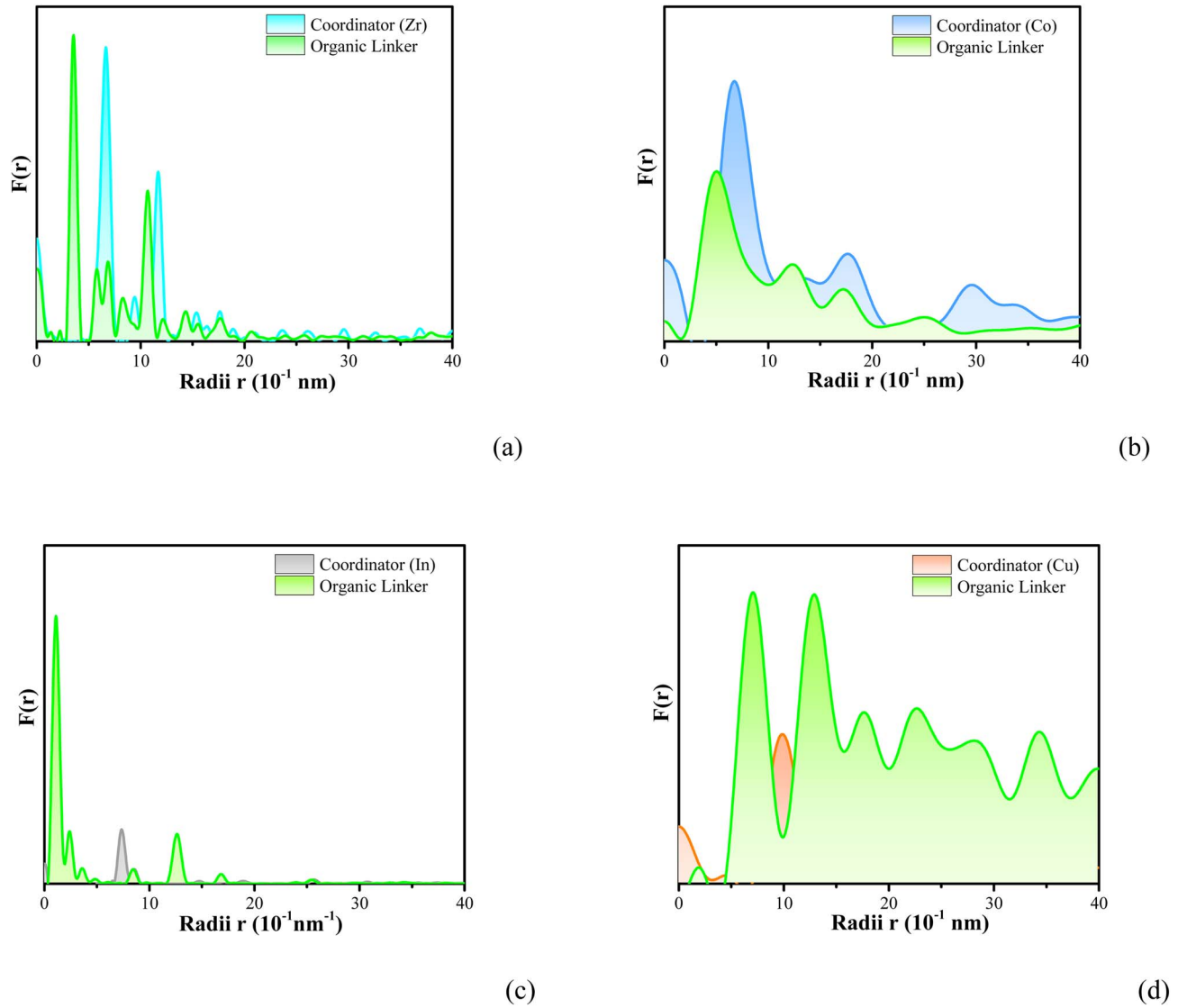

Fig. 2 The damping oscillation function $F(r)$ of the OL coordinated with metal. The green area represents the oscillatory distribution of the OL region. Cyan, blue, silver gray, and orange represent the oscillatory distributions of Zr (a), Co (b), In (c), and Cu (d), respectively.

Table 1 Applicable parameters of the damping oscillating function

$F(r)$	k	σ	r
Zr	0.415	0.22	8.95
Co	0.596	0.41	6.78
In	0.226	0.39	2.13
Cu	0.614	0.15	11.07

varying the effective potential under the specified conditions. Fig. 2 illustrates the evolution in the distances and positions between MCs and OLs in a quasi MOF as hydrogen molecules enter the structure. Our results indicate that the positions of hydrogen atoms in the four samples differ significantly from those of their corresponding MCs and OLs. Consequently, each particle within the simulated system occupies a series of continuous potential wells, corresponding to a broad parameter space, which increases the activity space of the hydrogen molecules inside the structure. Simulations were performed using our candidate metallic coordinators in the quasi-MOF sample, which is speculated to adopt a monoclinic or triclinic configuration within the quasi-crystalline system. Charge characteristics—whether positive or negative—along with variations in orbital distance, lead to particle charging or relocation. Furthermore, in the present study, the introduction of additional nuclei to the MCs and OLs, and the application of surface constraints on the quasi-MOF structure did not suppress or prevent the formation of other defects. Hydrogen molecules have a larger activity space in the cobalt- and copper-based samples, while their activity ability is weaker in the indium- and zirconium-based samples.

To further investigate the positional changes of hydrogen molecules relative to the MCs and OLs, we employed a CG scheme to macroscopically modulate the arrangements of MCs

Table 2 Summary of the low-pressure hydrogen adsorption capacities of selected MOFs at 77–298 K

MOF	BET ($m^2\ g^{-1}$)	Langmuir ($m^2\ g^{-1}$)	Pore volume ($cm^3\ g^{-1}$)	Uptake capacity (mmol g^{-1})	Pressure (bar)	Temperature (K)	Ref.
Mg-MOF-74	1495	1905	0.411	8.00	1	296	62
Co-MOF-74	1357	1688	0.487	5.66	1	77	63
En-MOF-74	1253	1270	0.392	4.57	1	298	64
QI-Cu	1631	1863	0.662	4.56	1	77	65
HKUST-1	803	1492	0.522	4.18	1	298	66
MPM-1-TIFSIX	840	1035	0.314	4.00	1	298	67
NU-1101	2522	2847	1.014	3.93	1	293	68
Zr-based MOF sample	1089	2251	0.709	4.12	1	77	This work
Co-based MOF sample	344	448	0.137	3.28	1	77	This work
In-based MOF sample	1286	1520	0.483	5.25	1	77	This work
Cu-based MOF sample	898	962	0.291	4.35	1	77	This work

and OLs, as illustrated in Fig. 3(a)–(d). This approach yielded the corresponding framework structures through symmetric operations based on rhombic, hexagonal, octagonal, and square motifs. Detailed analysis detected measurable structural strain across three or more coordination variants of the metal centers in these samples.[51] Furthermore, the resulting structures exhibit topological characteristics enabled by a semi-orthogonal approximation derived from the layout system, which can well accommodate hydrogen molecules on other vacancies. We characterized these quasi-MOF samples using lateral crystal structure diffraction. The resulting diffraction patterns displayed several distributed Bragg reflector characteristic features.[52,53] A common trait among these patterns is the outward diffusion of diffraction intensity from the central region, all exhibiting uniform orientation. The three-dimensional structures corresponding to these Bragg distributions are presented in Fig. 3(e)–(h). Our analysis indicates that these architectures are predominantly governed by the geometric extent of the grouped spherical shells, which also induce corresponding spatial dislocations. These spherical shells contain a large number of voids and interstitial particles, indicating the presence of numerous voids in actual space and facilitating the escape of hydrogen molecules from the structure.

The projection of the particles along the axis of symmetry exhibits periodic tiling characteristics, and this texture distribution can give high-density embedded pores. The separation between these two directions follows the Fibonacci sequence and enriches the remaining particle distribution through evenly spaced connection points over long distances.[54] Through visual inspection, it was confirmed that the particle-free regions of the zirconium and cobalt samples are at an angle of 30° to the normal direction, while those of indium and copper samples are at 22.5° and 45° angles, respectively, indicating topological differences in their actual structures. A parallel generative density function $G(r)$[55,56] (as revealed in Fig. 3) was deployed to statistically model the probability for CG processed particles with conjunction number n and distance d in time τ.

$$G(r) = \frac{1}{r^{15}} + \frac{1}{r^{3}} \cos\ \tau(n(r - 1.25) - d) \quad (3)$$

This can be used to statistically determine the activity probability of adsorbed gas molecules based on the coordination number and discrete distance of particles. *Via* folding symmetry, it can be observed that these CG structures exhibit some structural reversals, providing a diffusion mechanism for hydrogen atoms moving internally, prioritizing the repositioning of the structure under the action of hydrogen molecules, especially those particles located at the MC and OL positions on quasi-MOF vacancies.

The eight structural types with the Schoenflies symbols of the quasi-MOFs model mentioned above were used to normalize the position coordinate conformation as shown in Fig. 4, in order to demonstrate the relationship between hydrogen storage performance and topological structure. These were combined with the generated density function $G(r)$ to identify the point group (PG) of each CG sample within its target polyhedral region. We used the PG distribution of the CG samples to obtain information on the movement of adsorbed hydrogen molecules. By analyzing the PG schematic diagram, the structures were divided into eight tetragonal forms: D_{2h}, C_{4v}, C_{6v}, D_{6h}, D_{3h}, C_{2v}, C_{2h}, and C_{4h}, corresponding to the zirconium-, cobalt-, indium-, and copper-based samples, respectively. The D_{2h} and C_{4v} PG correspond to the tetragonal dense packing structure $(ZrO_4)^{4-}$ and $(InO_4)^{2-}$ polyhedra formed by ZrO. The tetrahedral coordination groups C_{2v}, C_{2h}, and C_{4h} have been observed in both experimental and simulated structures. Through MD calculations of orbital localization based on the MOF-74 and ZIF-8 variant models, small deviations were discovered, allowing for the determination of the activity of the hydrogen molecules in the cavity. These structures can be described as periodic interpenetrating cubic autohedra, which contain dodecahedral $(CoO)^{-}$, $(CuO)^{-}$, and $(CuO)_3^{-}$ units sharing the same edges as CoO and can form equiaxed structures consistent with hydrogen atoms at spatial sites. The D_{6h} structure $(InO_4)^{3-}$ and C_{6v} structure $(InO_3)_2^{3-}$ are single-atom chains formed during isotropic and anisotropic grain simulation, which can capture the position of the hydrogen atoms to a greater extent.

After observing the interior of these main CG structures, we found that they are always characterized by symmetrical centers

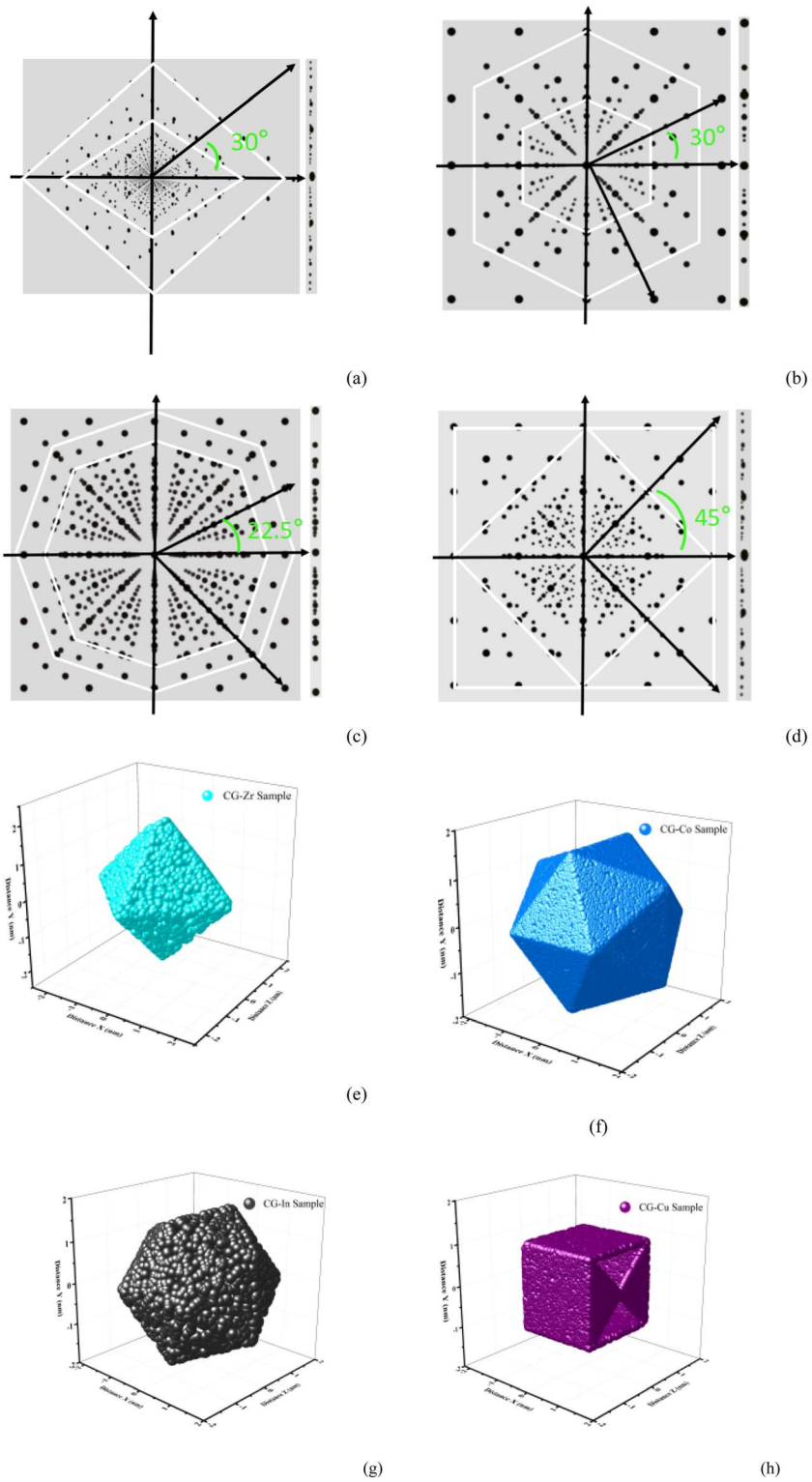

Fig. 3 CG models and their distributions of the quasi-MOF structure; (a) Zr-based sample and its structural distribution, (b) Co-based sample and its structural distribution, (c) is the In-based sample and its structural distribution, and (d) is the Cu-based sample and its structural distribution. Potential parameters for these figures are $(n, d, \tau) = (4.25, 0.72, 0.05)$. Gaseous spherical solid formed by CG isotropic particles for Zr, Co, In and Cu (shown in cyan (e), silver-gray (f), blue (g) and dark purple (h)). The whole system contains 2000 particles.

under PG partitioning and exhibit a tightly packed bilayer arrangement, which can be used to divide them into specific regions of hydrogen adsorption. For example, the C_{2v} symmetry of the Zr samples exhibits instability in the coordinate system, indicating that it may form polycrystals under high-pressure phase conditions. In this way, by combining the particle

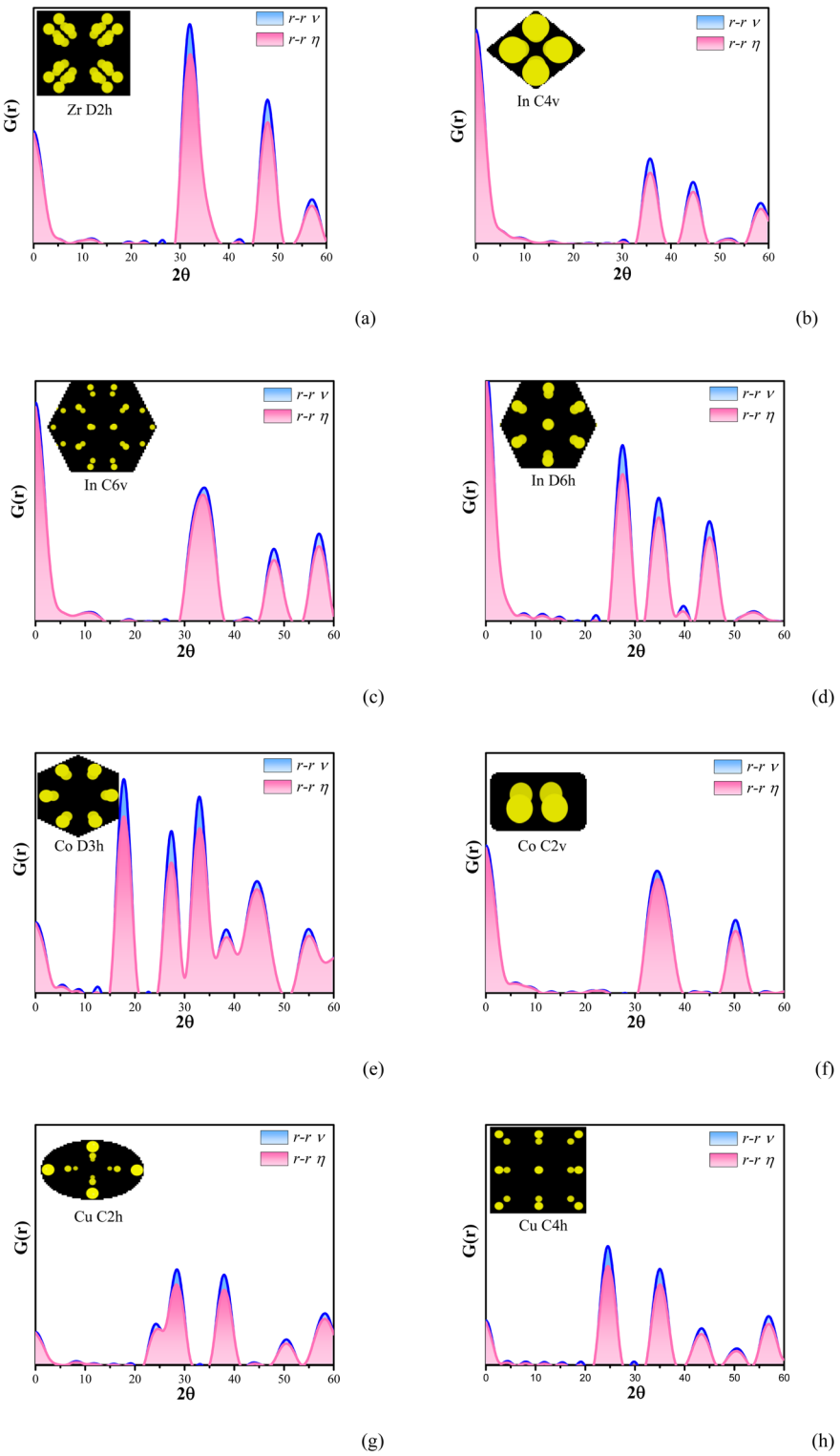

Fig. 4 Grain coordination distribution of the quasi-MOF crystals with approximate crystal phases and the scanning curve of hydrogen molecules moving inside the quasi-MOF. The position mode of hydrogen molecule movement is divided into horizontal ($r - r\ \eta$) and vertical ($r - r\ \nu$) directions entering the polyhedral region. The distribution of coarse particle positions corresponding to the peak area generated by $G(r)$ is marked in the figure, for the Zr-containing sample (a), In-containing sample (b)–(d), Co-containing sample (e)–(f), and Cu-containing sample (g)–(h).

distribution patterns in both the horizontal and vertical directions, it is easier to obtain a bilayer quasi-MOF structure. The C_{2h}, C_{4h}, and D_{6h} symmetries exhibited by the Cu and In samples may induce the formation of chiral groups, thereby promoting the formation of hydrogen adsorption vacancies. However, in the process of point symmetry evolution, the

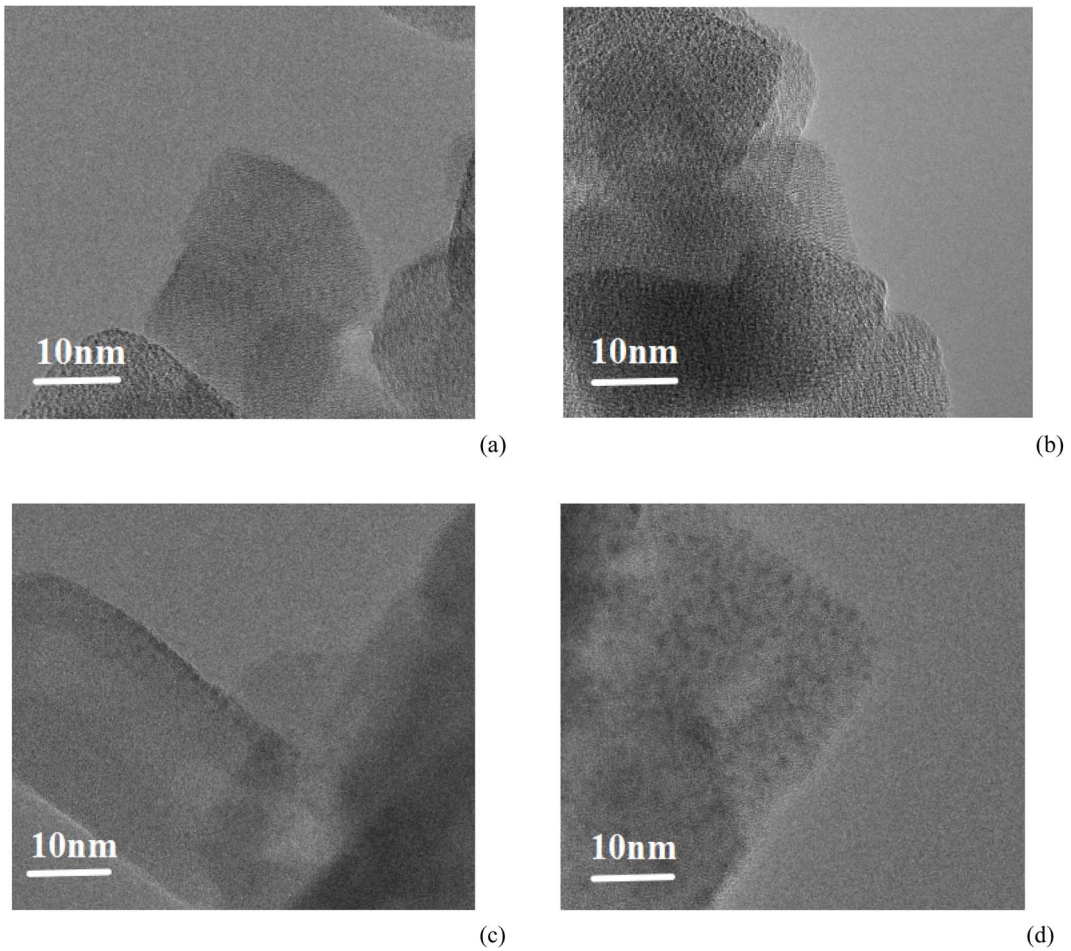

Fig. 5 Transmission electron microscope (TEM) images of the MOF samples, showing different types of missing structure defects. (a) TEM characterization of Zr-based MOF, (b) TEM characterization of Co-based MOF, (c) TEM characterization of In-based MOF, (d) TEM characterization of Cu-based MOF.

elimination of inserted symmetry elements can lead to inconsistent symmetry between adjacent regions, resulting in different positions for hydrogen atoms to enter vacancies. It is worth noting that the comprehensive analysis of regular reciprocal space reveals the D_{3h} structure of the Co samples and the C_{2h} structure of the Cu samples, indicating that the enhanced grain boundary strengthening mechanism contributes to structural stability and can stabilize the escape of hydrogen molecules. Using these samples as a reference, the tetragonal crystal system (Zr-based samples) may exhibit enhanced alternating composite peaks at wide diffraction angles ($2\theta > 45°$), while the hexagonal crystal system (Co- and In-based samples) exhibits enhanced alternating peaks at lower angles ($20° < 2\theta < 30°$). This unique scattering behavior reflects topological patterns related to the configuration and structure of the foldable lattice, which facilitates the reacquisition of hydrogen by absorbing vacancies.

Transmission electron microscopy is a practical tool to visualize the details of the defects of our MOF samples. The morphology and distribution were imaged by utilizing defects as sites for the formation emissive products that serve as markers (Fig. 5). Ordered missing OL and OL cluster defects were imaged, and these two defects coexists. Since our MOF structure was more stable, direct images with the subunit crystal cell were obtained. We also performed selective area electron diffraction (SAED) scanning on these sample structures (results are shown in Fig. S1.)

Guided by the distribution pattern of joint sites from electron microscopy (Fig. 5 and 6a–h), we proposed a series of compositional structures. Among them, distribution rules and presentation forms with the same coordination indicated that the Co and Zr sample have a spherical and skirt-shaped morphology, while only complete block and lamellar structures were observed in In and Cu. As mentioned earlier, there were no corresponding effective peaks observed for $F(r)$ and $G(r)$, thus confirming that the Co and Zr samples can form a consistent equiaxed structure with the organic compounds in this work. By marking the wide-angle diffraction range of Co atoms and Cu atoms through perspective breakdown,[57] it was found that there is a close relationship between them (compared with that of the Cu sample, the effective coordination of the Co atoms exhibited similar MPP character within the 0–25° diffraction angle range as reflected in the $G(r)$ function; hence, we conclude that the Cu and Co sample here have the

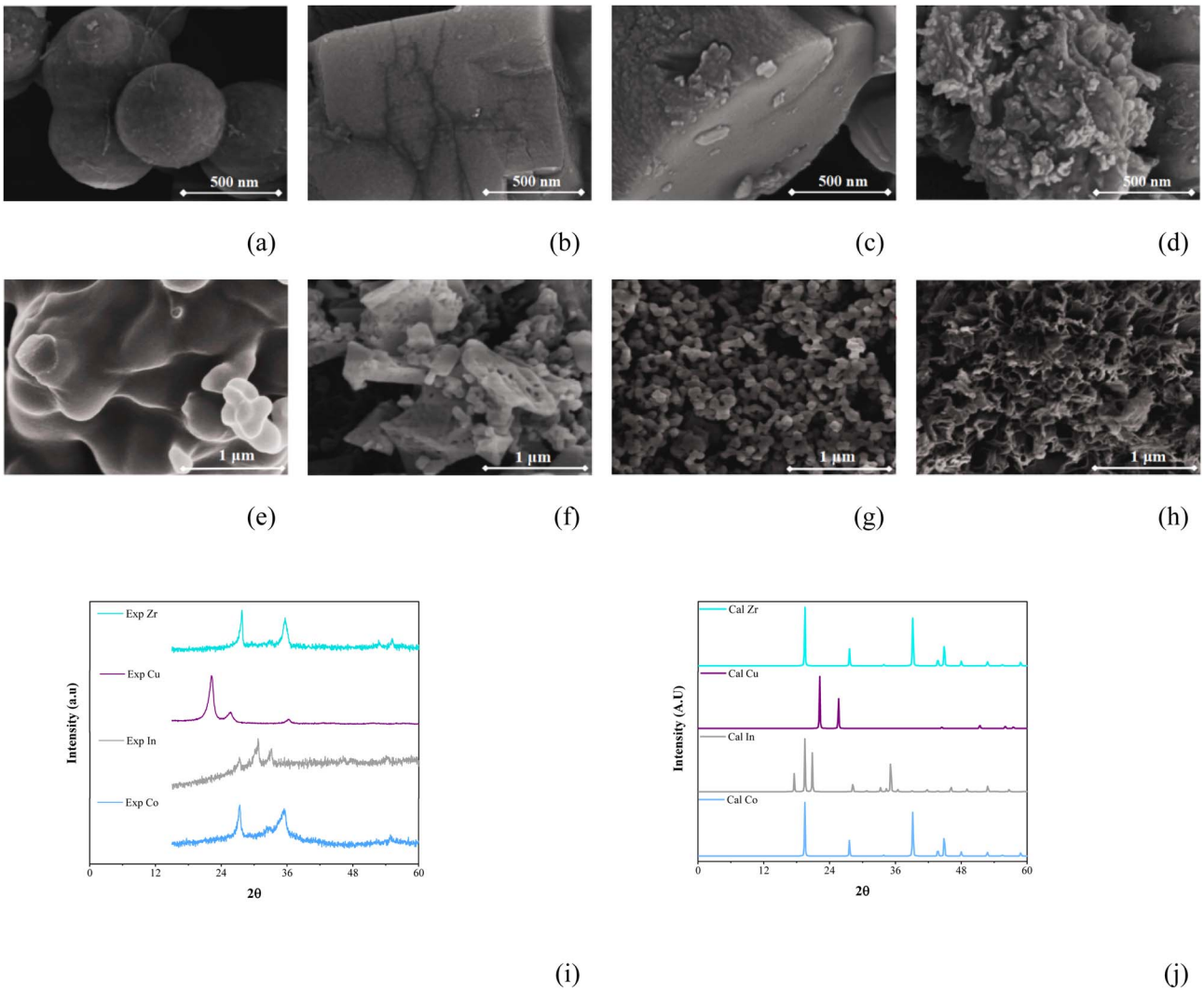

Fig. 6 Scanning electron microscopy (SEM) images (a)–(h), experimental X-ray diffraction (XRD) patterns (i), and simulated XRD patterns (i)–(j). (a) and (e) Zr sample and its surface morphologies; (b) and (f) In sample and its surface morphologies; (c) and (g) Co sample and its surface morphologies; (d) and (h) Cu sample and its surface morphologies. (i) Experimental XRD diffraction patterns. (j) XRD diffraction patterns based on the simulated structures.

same valence state to fill the atoms in the vacancies). Through the calibration of the face-centered decahedral criterion, the effective atomic coordination generated by Co atoms in different valence states can more easily form microporous structures with O atoms on organic linking agents. The staggered sizes of the micropores and the order of their connections illustrated in the figure indicate that the Co sample has more coordination possibilities within the diffraction range of <10°. Approximately and accidentally, when the diffraction angle is greater than or equal to the perspective angle at the homologous position, the In atom can be seen to have an enhanced signal on the basis of the same valence state as the Zr, Cu, and Co samples, or the atoms in these element arrays can be divided into structures within the same unit frame, indicating that In has the maximum coordination selection space and priority at this time.

We attempted to identify these structures using crystal diffraction methods, and compared the atomic arrays composed of the four candidate elements with the framework structures assembled with the OLs in the order of perspective diffraction peak analysis (Fig. 6(i) and (j)). It was observed that the peak formed by the In atomic array appeared at a relatively later position in the presence of OL, while some representative characteristic peaks did not appear in the diffraction pattern, such as the peak at 25° for Co atoms and the peak at 45° for Zr atoms (although they all have a valence state of +4). Due to the current deployment of anomalous dispersion coefficients only for commonly used X-ray anode wavelengths, we have modified the synchrotron radiation or changed the default wavelengths in our calculations to consider the introduction of anomalous dispersion. Subsequently, these signs of modification changed the structure of the split single box line; however, only a small amount of signal attenuation occurred in the Co atomic array

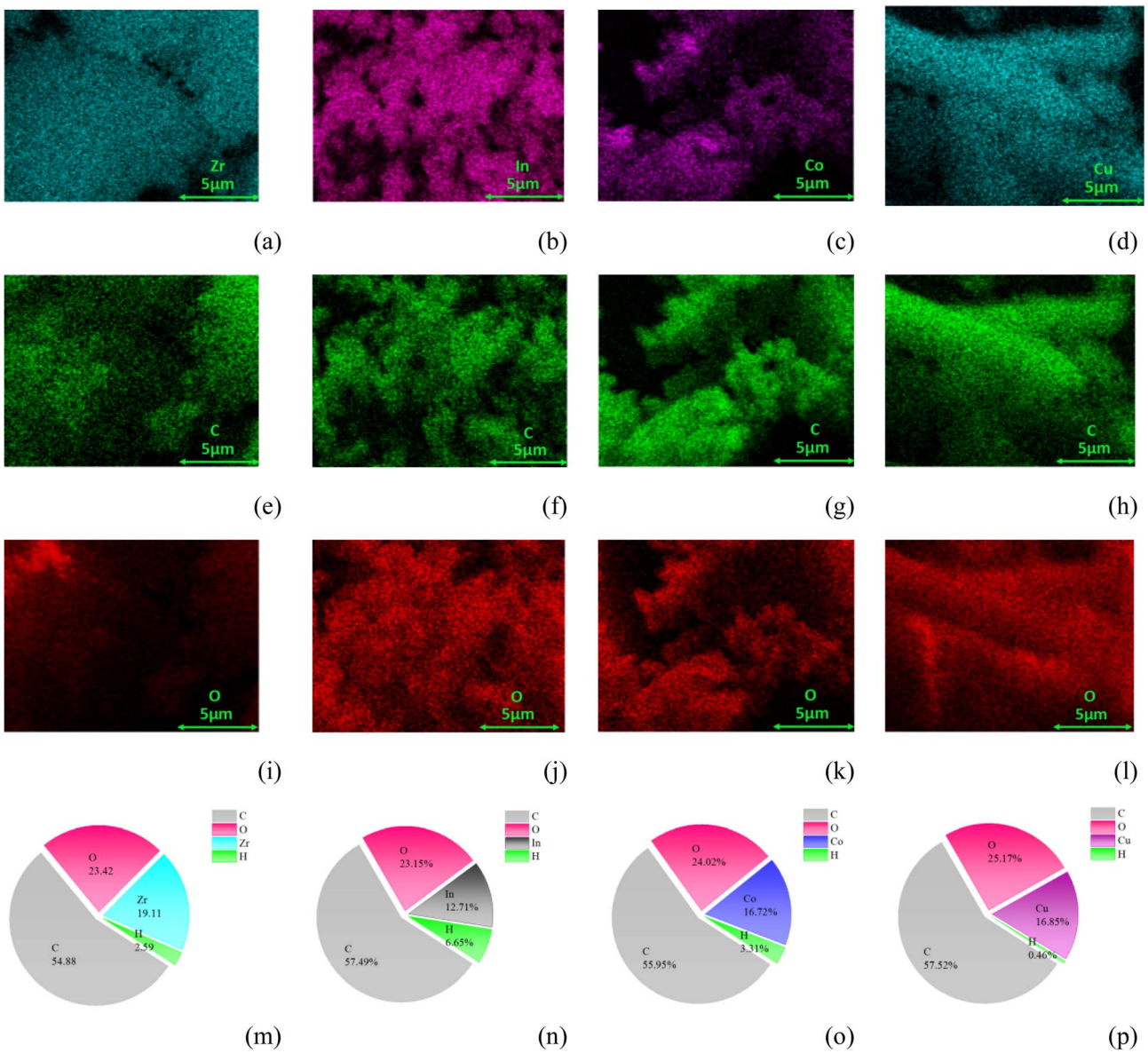

Fig. 7 Energy dispersive spectroscopy (EDS) (a)–(l) and elemental weight analysis (EWA) (m)–(p) of specified samples (Zr, Co, In, and Cu). For EDS, Zr and Cu are represented as cyan, In and Co are shown in dark pink, and C and O elements are shown in green ((e)–(h)) and red ((i)–(l)), respectively. For EWA, carbon is represented by light gray, oxygen is represented by pink, hydrogen is represented by green, and metal elements are represented by cyan (Zr, (m)), silver-gray (In, (n)), light blue (Co, (o)), and purple (Cu, (p)) in sequence.

and Cu atomic array. Through diffraction analysis with functional group structures, the same structural pattern as before was achieved; the experimental perspective diffraction angle should generally be 20° or more lower than that of a single atomic diffraction pattern. By vertically comparing the introduction of functional groups, atoms with higher valence states originating from the array are closer to the original diffraction patterns, such as the +6 (+3) valence of In, the +4 (+2) valence of the Co sample, and the +2 (+1) valence of the Cu sample. Associated with the direction shown in Fig. 2, the perspective diffraction of the Zr atomic array was detected by the crystal diffraction method, and it was found that the same diffraction morphology was maintained in the three directions of (1,0,0), (0,1,0), and (0,0,1) after introducing functional groups.

Four distinct modalities emerged around the fundamental framework samples in our synthesis route design, as visualized by elemental mapping *via* shaping scanning[58] and presented in Fig. 7. Atomization processes ejected reaction products from centrally enriched zones in our samples, with unclear coupling between adjacent regions during recycling. From the tenting exhibition of interatomic compositing, the elemental scanning analysis indicated that the metal cores have close contact with the oxycarbide matrix, however, except for the Zr sample, where the Zr atomic position overlaps with the carbon and oxygen bridges. We also employed the electronic signal probe, which indicated larger gaps between the layout of the elements cobalt and indium and their corresponding non-metallic element distribution on the surface of the preparative framework

sample. According to EDS analysis, the atomic distributions of Co (94.45%), In (93.15%), and Cu (95.78%) exhibit near-identical coverage ratios with the carbon and oxygen atoms, confirming the uniform preparation of the framework monomers. Zr (96.15%) dominates the appearance coordinate to substantially span the full size of the systematic formula sample, but only a few carbide decorators and oxygen overlays are exposed. The In sample and Cu sample formed oxycarbides in a 1 : 3 ratio within the primary bearing structure, which subsequently promoted aromatic group interactions, further increasing the carbide ratio to 1 : 6. This proportional occupancy enhancement amplified micropore formation, demonstrating latent structural benefits. Simultaneously, component analysis *via* EWA (elemental weight analysis) of the Co and In samples revealed deviations in the hydrogen ratio, indicating that certain coordination sites contain vacancies capable of retaining hydrogen atoms as either infilling species or due to bond-deficient alignment.

We conducted traversal scanning and element tracing analysis based on the composition and content ratio of our homoplasmic MOF-74 (Co, In, Cu) and UIO-66 (Zr) samples in this work. Carbon accounts for a large proportion the Zr sample. Therefore, the bilateral coordination of the benzene ring occupies the main binding form when the BDC belonging to the OL coordinates with metal salts. In addition, the small signal detected for the elements H and Co is stronger than that for O during the coordination, and the characteristic peak appears earlier than that of C, which identified the effective connection coordination in the Co sample. For the homoplasmic MOF-174 samples, only a small number of characteristic peaks of O and In appeared, and the signal intensity of C was weaker than that of the Co and Zr samples. With a fixed metal-to-OL (organic linker) coordination ratio of 1 : 3, the Cu sample exhibits distinct coordination behavior compared to the Co sample. While the Co system forms complex coordination structures, the Cu sample predominantly adopts a single coordination mode. Furthermore, in both the In and Co samples, the metal element signals appear earlier in the content rate than the characteristic oxygen, mirroring the behavior observed in the Cu system. However, the difference is that the signal of C in the In sample is obtained earlier than that of the Cu sample. From the perspective of distribution position, the distribution position of In should be closer to the inner position of the surrounding organic connection structure. Therefore, combining the theory of electron layer pairing and the theoretical analysis of Bohr electron layer pairs,[59] the elements Cu, Zr, and Co form a composite coordination form with O atoms in the form of 2-fold or 4-fold connections.[60,61]

The motion trajectory of hydrogen atoms analyzed using the quasi-Monte Carlo (qMC) algorithm indicates the presence of

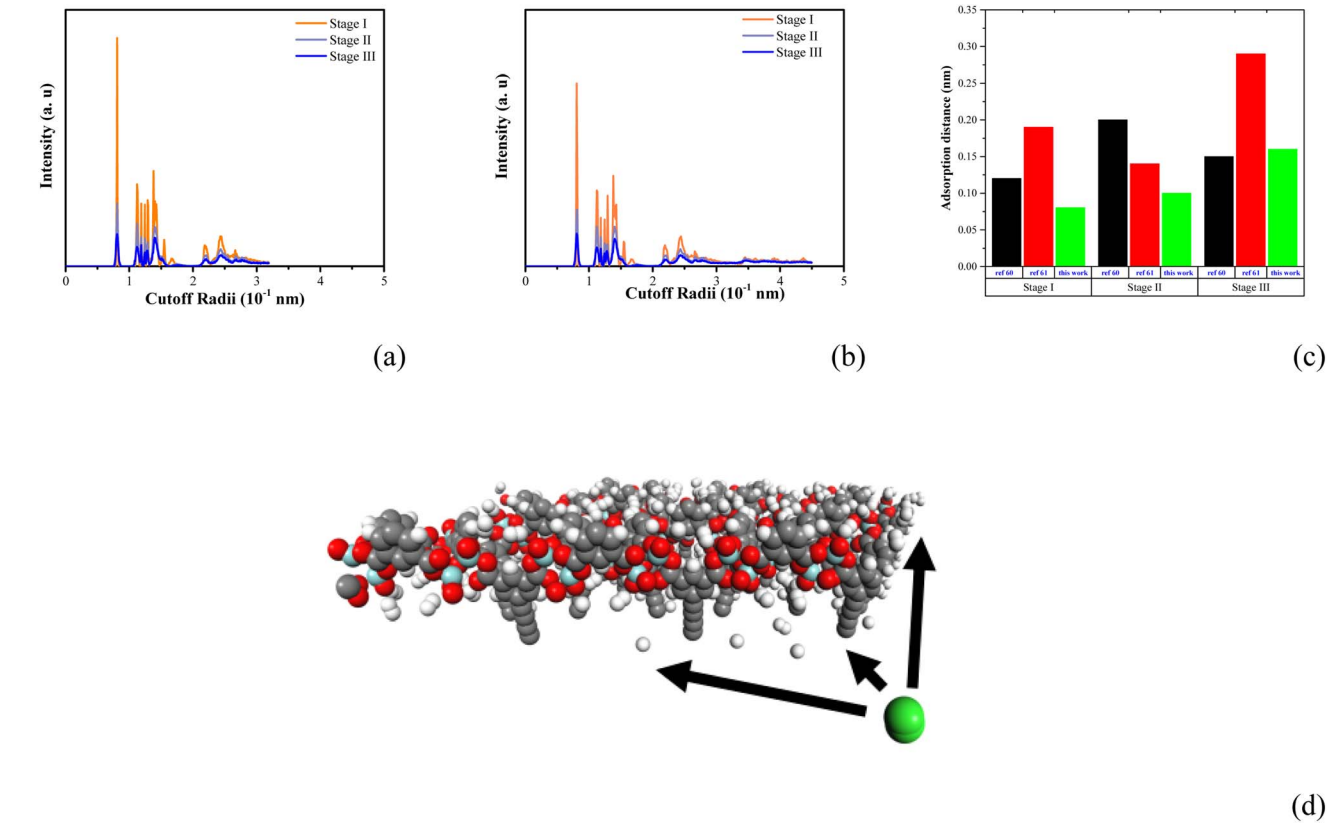

Fig. 8 Simulation of the dynamic detection between atoms before and after adsorption (a) and (b), average hydrogen bond statistics during the adsorption process (c), and atomic distribution during the equilibrium period (d). The first stage is the particle distribution state at the initial thermal equilibrium, the second stage is the particle distribution state during the heating process, and the third stage is the particle distribution state at high-temperature thermal equilibrium.

multiple connections during the thermal equilibrium (MD) process (see Fig. 8). In the initial stage, these bonds hinder interatomic displacement, causing other hydrogen atoms, delayed within the gaps of typical micropores, to move in opposite directions around the pore structure. As defects appear in the expanded pores within the porous matrix, the qMC algorithm also mitigates the weakened resonance effect between hydrogen atoms and OLs by avoiding interactions with non-critical atoms. Simulations using deployed tracer atoms to penetrate each feature cage revealed atomic oscillation behavior at low temperatures (79.35 K) under a relaxation pressure of 0.35 atm and intramolecular tension of 0.005 atm nm^{-1}. The aromatic ring undergoes compression and distortion, with its average diameter decreasing from 0.235 nm to 0.201 nm. This local contraction prevents further internalization of mobile hydrogen atoms around the coordination center, but promotes the formation of capillary chambers within each unit framework.

MD simulations can effectively capture the behavior and evolution of hydrogen atoms within quasi-MOF structures,

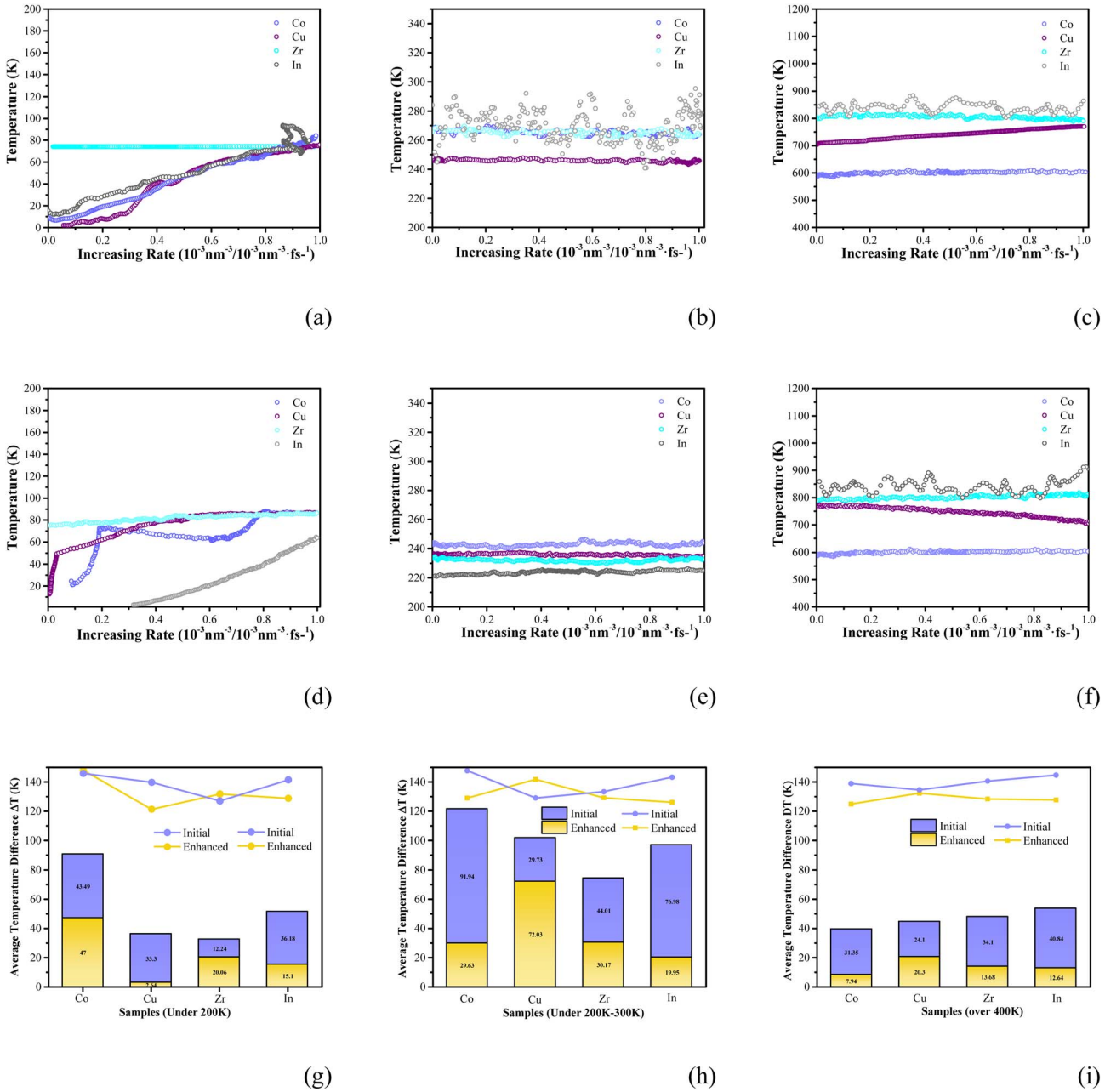

Fig. 9 Dynamic process and evaluation of gas adsorption with coordinated metals. (a)–(c) are universal atoms and hydrogen adsorption under normal conditions (0–200 K, 200–350 K, and over 400 K). (d)–(f) correspond to (a)–(c) and consider the dynamic MPP potential and density generation function $G(r)$ for hydrogen adsorption. (g)–(i) represent the degree of enhancement/weakening of hydrogen adsorption after the gas adsorption process, where yellow represents the enhancement/weakening of hydrogen adsorption when using universal atoms, and blue represents the enhanced/weakened hydrogen adsorption after using MPP and $G(r)$.

enabling detailed tracking and analysis of potential reactive processes occurring inside the cavities of these materials. We conducted a trajectory analysis of hydrogen atoms throughout the MD simulation, calibrating their positions before and after adsorption and monitoring their behavior during the adsorption process. By examining motion patterns based on the activation distances of distinct characteristic atoms, along with subtle relaxation behaviors, it was determined that hydrogen atoms located between the MC and OL regions remain stabilized at a fixed distance of approximately 0.3 nm. Based on the movement of hydrogen atoms within the MC and OL environments, the process can be categorized into three stages. As shown in Fig. 8(a) and (b), the first stage involves a strong binding interaction (0.07–0.08 nm) with coherent coordination during the movement of hydrogen atoms within the OL layer, guided by bonding rules. In the second stage (thermal equilibrium), the average partial bonding distance ranges between 0.10–0.15 nm, reflecting the stable migration of hydrogen atoms within the pore spaces. During the third stage, thermal fluctuations lead to a reduction in interaction strength, and hydrogen atoms become dispersed as the interlayer spacing in the OL structure increases. This stage mobilizes loosely bound atoms, resulting in a displacement of hydrogen atoms at 0.245 nm in the original structure, compared to 0.220 nm under thermal equilibrium. In addition, the number of hydrogen bonds in the pores was quantified by introducing comparative references (Fig. 8(c)), revealing the trend of free hydrogen atoms forming hydrogen bonds during the adsorption process. No corresponding reaction characteristics were detected within the simulated calibration range.

We defined the gas molecular volume per unit cell volume as a dynamic absorption metric, and measured it across three

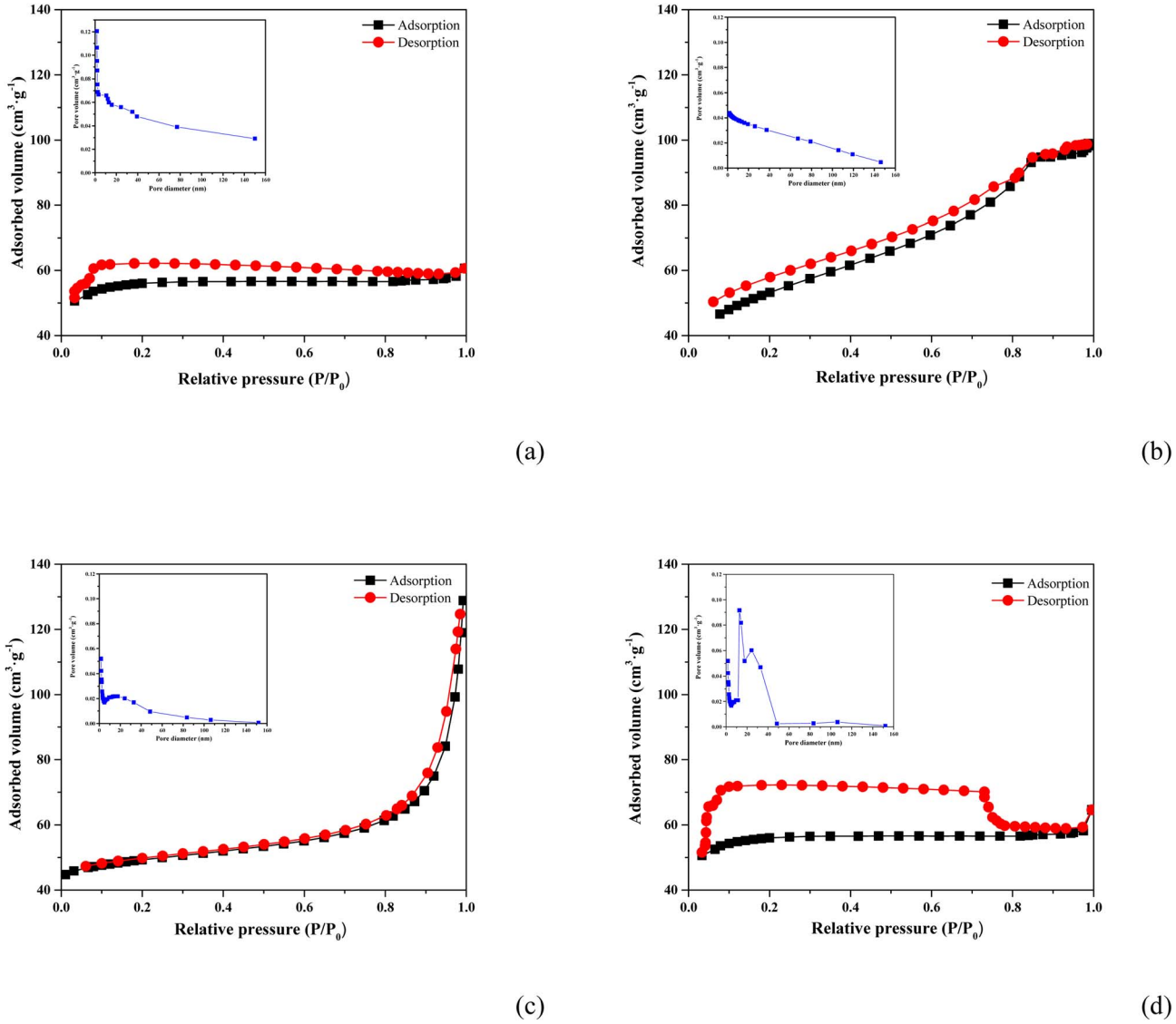

Fig. 10 N_2 isotherm at 77 K and 1 bar and pore size distribution (insets). (a) BET curve and pore distribution of Zr-based MOF samples, (b) BET curve and pore distribution of Co-based MOF samples, (c) BET curve and pore distribution of In-based MOF samples, (d) BET curve and pore distribution of Cu-based MOF samples.

temperature regimes (0–200 K, 200–300 K, and >400 K) in tablet specimens, as shown in Fig. 9. By searching broadly across the low-temperature range, two floating changes occurred in the single Zr-based framework monomer sample (FMS) at 72.29 K and 87.68 K with a gas volume coverage rate (GVCR) of 0.19 × 10^{-3} $nm^{-3}/10^{-3}$ nm^{-3} fs^{-1} and 0.8 × 10^{-3} $nm^{-3}/10^{-3}$ nm^{-3} fs^{-1}, respectively; however, the GVCR did not exceed 0.42 × 10^{-3} $nm^{-3}/10^{-3}$ nm^{-3} fs^{-1} at 74 K for the corresponding framework compositing coating sample (FCCS). The same behavior appeared on the positive correlation trend of temperature and GVCR for the other three coated samples without an annealing method applied. The thermal relaxation proceeded through three units of simulation time (30 ps) until the arc-shaped buffer point appeared at 50 K for the single Co-based FMS; nevertheless, at a temperature of around 50 K, the GVCR has exceeded half the volume in the unit framework structure for the cobalt FCCS. Additionally, we did not observe any other negative responses between indium and copper throughout the entire hypothermia process of the simulation, from the monomer samples to their composite samples.

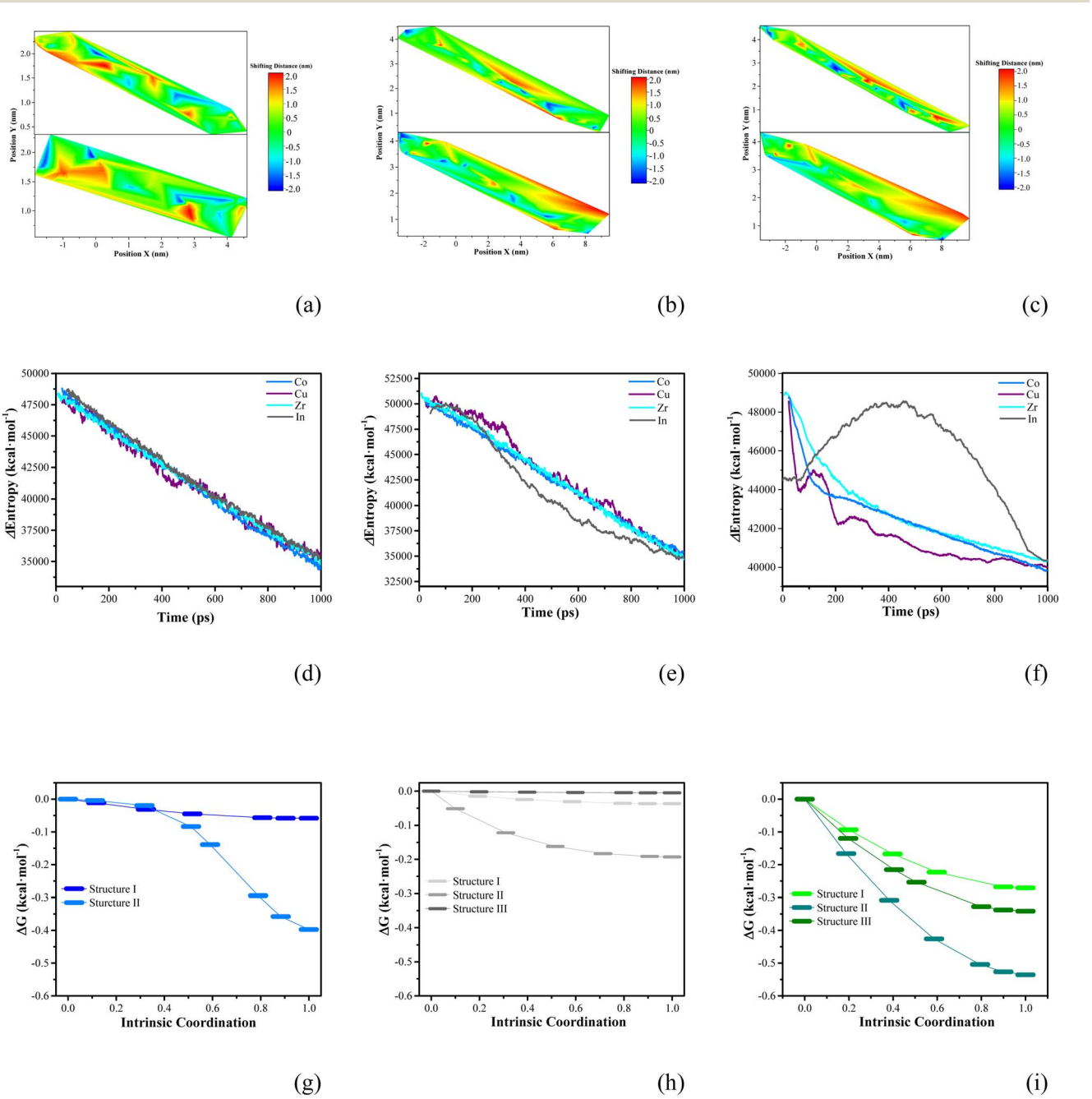

Fig. 11 Changes in system energy during the hydrogen adsorption process. (a)–(c) Movement of hydrogen particles at the corresponding top view angles when the OL is BDC, BPDC, and TPDC, respectively. (d)–(f) Overall energy changes during the hydrogen adsorption process; the OLs corresponding to (d)–(f) are BDC, BPDC, and TPDC. (g)–(i) Transition state energy change corresponding to the change of the target OL in the system, where Structure I is BDC, Structure II is BPDC, and Structure III is TPDC.

Notably, the In-based FMS exhibited significant temperature variations averaging between 240 K and 295 K, while the In-based FCCS maintained a stable oscillatory pattern from 808 K to 883 K.

The porous structures of the Zr sample, Co sample, In sample and Cu sample were analyzed *via* N_2 sorption measurements. As shown in Fig. 10, the Brunauer–Emmett–Teller surface area of the In sample is 1286 $m^2\ g^{-1}$, which is higher than that of the Zr sample (1089 $m^2\ g^{-1}$), Co sample (344 $m^2\ g^{-1}$), and Cu sample (898 $m^2\ g^{-1}$), indicating that the introduction of mesopores and macropores reduces the specific surface area of the particles. We also calculated the BET and pore distribution of the control group with BPDC and TPDC as OLs, as shown in Fig. S2 and Table S1. Due to the prepared quasi-MOF templates having a size of approximately 50–200 nm, their removal left many large pores in the sample, as can be seen from the SEM images (Fig. 6(a)–(h)). A comparison with the literature was carried out, and the relevant data statistics are provided in Table 2. The pore size distribution of the samples tested using that BJH and DFT methods (Fig. 10(a)–(d)) also indicates that the main pore sizes are below 2 nm in the Zr samples, In samples, and Cu samples. In the pore distribution of the Co samples, the presence of mesopores and macropores is obvious. These mesopores and macropores lead to a decrease in BET values.

To explain the series of indeterminate phenomenon that occurred with adsorption, we captured the dynamic details for these samples and attempted to sketch outlines of the entire process. During the adsorption process shown above, we used simulated dynamic traversal methods based on MD and qMC, as well as the density of gas molecules within the framework structure. We calculated statistical data on the distribution of hydrogen molecules labeled with movable atoms and marked with long tube approaches. Based on the scale of hydrogen

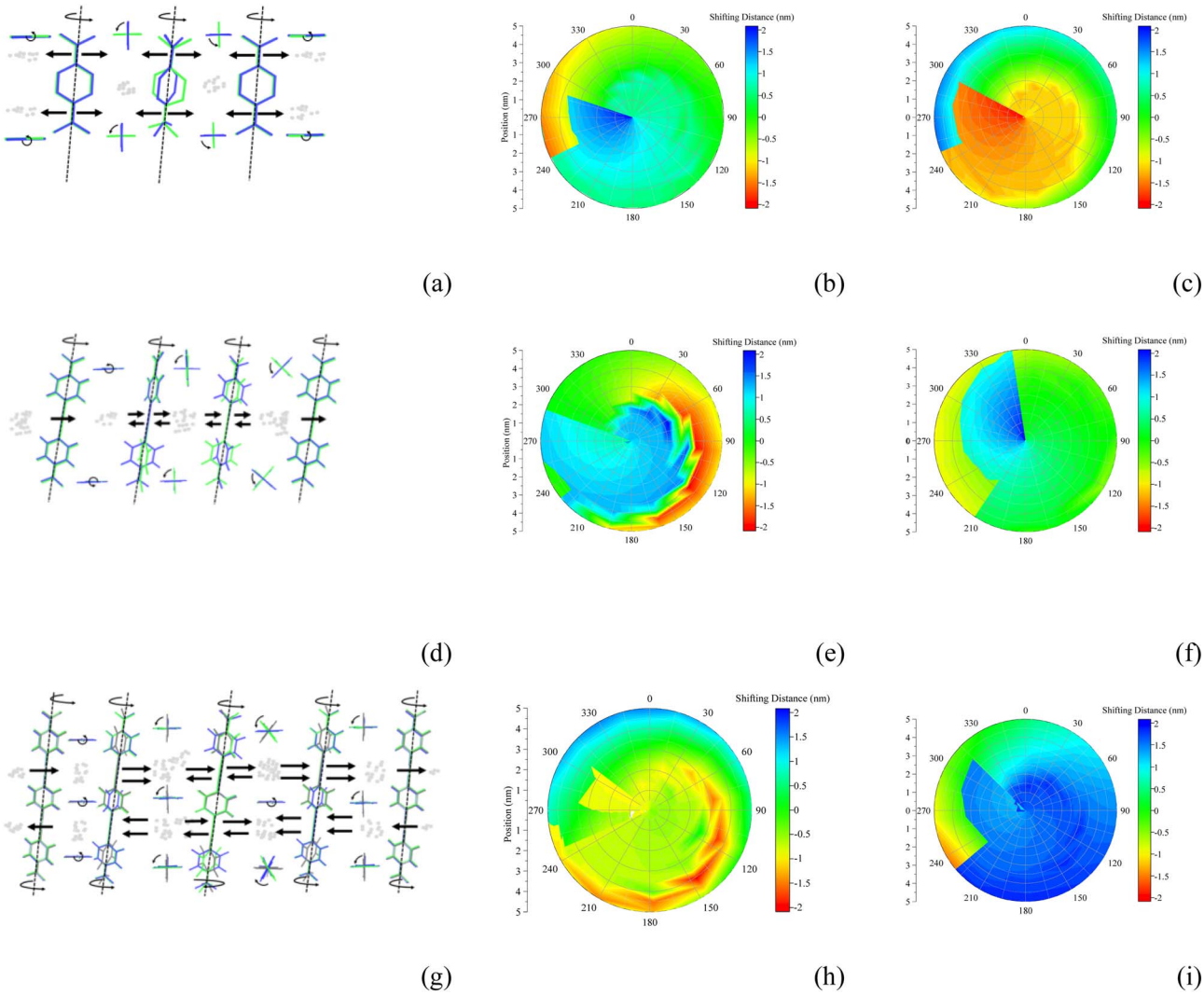

Fig. 12 Changes in hydrogen molecules and OLs during hydrogen adsorption. (a), (d) and (g) Mechanisms of interaction between the gas molecules and corresponding changes in BDC, BPDC, and TPDC during the adsorption process. (b), (e) and (h) Displacement changes of hydrogen particles under the horizontal angle of view corresponding to (a), (d), and (g) with the conditions of general atomic simulation and half cycle simulation time. (c) (f) and (i) Displacement changes of hydrogen particles under the horizontal angle of view corresponding to (a), (d) and (g) with the conditions of MPP potential, $G(r)$ simulation and half cycle simulation.

molecules formed inside the microporous chamber and the displacement of particles per unit time, we divided the gas flow direction and storage channels (the description of these channels is based on the first frame of gas entering the sample micropores, as shown in Fig. 11(a)–(c) and Fig. S3). From the trends shown in the graph, these channels are organized into manifestations with unidirectional flow, multiple parallelism, geometric misalignment, and spatial intersection characteristics. The binding coordination samples with Zr as the core, as well as the samples with Co and In as the core, have universality for gas permeation, but the Zr sample can effectively suppress the collapse of the gas channel by forming a single gas channel, thus presenting a larger main channel in the form of a single branch. The divergent channels in the Co samples utilize the more compact OL support structure to release more gas, forming storage nodes in which more gas molecules can remain. However, there are no reliable support channels in the branch channels of the In samples, resulting in only a small amount of hydrogen particles being stored and rapidly passing through these enclosed spaces, which are smaller than the Co sample storage nodes. In the gas multiple dislocation channels formed by the Cu sample, we detected gas accumulation at the edge of the Cu sample framework structure and only observed a small amount of gas retention at the middle position of the framework structure, on the same channel path and repeated particle motion trajectories, as well as observing the dense distribution of gas flow. These hydrogen storage positions also deviated within the range of 0.5–1 nm as the simulation progressed. When the gas molecules gathered in the middle of the framework, the hydrogen particles passing through different transmission routes compared to those in the Zr, Co and In samples manifested in annular gaps with diameters of less than 0.415 nm and greater than 0.604 nm, respectively. We also compared the experimental results of the adsorption process (see Fig. S4).

To quantitatively analyze these structural responses, we evaluated the effective changes in hydrogen particle density relative to the organic linker (OL) by calculating the statistical entropy (SE) for each sample during the simulations (detailed SE calculation methods are provided in Text S1 of the SI). As shown in Fig. 11(d)–(i), we correlated the hydrogen particle population density with the instantaneous OL deformation displacement (per unit simulation time). The transition state energies for OL deformations were computed and analyzed for all candidate linkers (Fig. S5). During framework organization, the hydrogen particle occupation of micropores (4–6 nm) and cavities (3–8 nm) induces steric repulsion with the BDC/BPDC/TPDC linkers, leading to significant axial torsion of the OL units. This torsional deformation subsequently modulates gas molecule diffusion within the porous network.

The changes in the adsorption process of the hydrogen molecules in the structural pore cavity are shown in Fig. 11 and 12. When the OL branch twists, the SE of hydrogen particles in the micropores is much smaller than that in the cavity. When the OL does not twist or only expands and contracts, the SE of hydrogen particles in the micropores is similar to that in the cavity, indicating that the helical strain field formed by axial twisting effectively reduces the hydrogen diffusion barrier, corresponding to faster hydrogen absorption and release rates. The topological defects introduced by OL branch twisting create a large number of adsorption sites with suitable binding energies, breaking through the limitations of low hydrogen storage capacity in the sample and corresponding to the kinetic stability of hydrogen adsorption. When the SE of the hydrogen particles reaches its minimum value of 0.25 kcal mol^{-1}, the twist angle between the benzene rings of BPDC and TPDC approaches 90°, indicating that hydrogen molecules are transferring into the cavity (hydrogen transfer). As thermal relaxation progresses to the intermediate stage, the OL is subjected to both axial and bilateral torsion, which is positively correlated with gas molecule absorption or dissipation, and at this time, hydrogen molecules are located stably inside the pore cavity (hydrogen relaxation). When the bilateral torsion reaches 46.7°, the SE of the hydrogen particles is below the valley value of 0.17 kcal mol^{-1} in the early stage. The energy difference between the OL transition state saddle point twisted at both ends and the SE is greater than that of the saddle point twisted at both ends in the middle. The distribution of hydrogen particles corresponding to SE is mainly located in the middle of the sample. In the final stage of the simulation, the distortion angle of the sample returned to its initial state, but the residual HP in the micropores and chambers caused the SE to exceed those of the initial and intermediate stages by 0.05 kcal mol^{-1} and 0.07 kcal mol^{-1}, respectively (hydrogen escape), in terms of quantity. All structural deformations observed in the simulation exhibit good reversibility after hydrogen desorption, indicating that these materials have good cycling stability.

Conclusion

Through controlled damping oscillations utilizing mixing-disturbance potentials, we successfully obtained mixed coordination MOFs with In/Co-based tetrahedral/octahedral elements and tetrahedral Zr/Cu-based elements. Under vibrational conversion, Co and In additionally formed hexahedral structures as their dominant coordination forms, exhibiting a preferential clockwise morphological orientation. In and Cu further displayed potential additional coordination sites within their high-valence arrays, which could provide potential excess hydrogen adsorption sites. Experimental and simulation results revealed that the In-based sample achieved a 12.3% hydrogen adsorption capacity across temperature gradients under theoretical conditions while maintaining high structural integrity and the highest adsorption performance among all the samples. No reactions were observed in any samples throughout the simulations. In contrast, Cu-based samples showed high thermal sensitivity, with hydrogen transport predominantly slowing or stagnating at structural edges. The In-based sample exhibits high structural integrity and has the highest hydrogen adsorption capacity among the four samples. Hydrogen adsorption can be effectively modulated by varying the number of benzene rings on the coordinated OL, as increased aromaticity enhances hydrogen permeability. Hydrogen mobility peaked at an inter-ring OL angle of 90° and showed a minimum at 45°, concurrently reaching maximum storage capacity. Furthermore, the variation in coordination

numbers at intermediate metal sites, such as Zr, Co, and In, facilitates the migration and diffusion of hydrogen molecules through the internal pore network of the framework. These findings position our materials as promising candidates for hydrogen adsorption and separation applications.

Methodologies

Experiment section

Experimental chemicals. Benzoic acid, dilute nitric acid, zirconia, cuprous oxide, and indium hydroxide (analytical grade, >99.5%) were purchased from J&K Scientific Co., Ltd. Copper oxide and cobalt hydroxide, ethanol solvent, *N*,*N*-dimethylformamide (DMF) solution, 1,2-dimethylcyclohexane, BDC, BPDC and TPDC (analytical grade, >99.7%) were purchased from Innochem Co., Ltd. All reagents were used directly without further purification. Deionized water used for testing was obtained from the deionization generator.

Preparation of synthesized MOF-like structures. Specifically, we dissolved 0.5 mol of the above-mentioned metal containing oxides and hydroxides in 25 ml of deionized water, and then added 0.1 M, 0.05 M, and 0.025 M ethanol solutions of BDC, BPDC, and TPDC to the above aqueous solutions. After mixing in 0.01 M dilute nitric acid, we stirred the mixtures for 30 min and then heated and stirred them in a thermal radiation reactor for 24 h.

Instrument parameters and working conditions. Structural relaxation characterization for the experimental samples was directly monitored and processed using SHELXT with the assistance of SHELXL and OLEX-2. XRD images and model rules were determined using PANALYTICAL Empyrean X-ray diffractometer equipped with monochromatic Cu Kα radiation units (40 kV, 40 mA) and a PixCel^{3D} detector. The microstructure of the samples was observed using a Hitachi SU 8600 scanning electronic microscope under acceleration voltages of 5 kV, 10 kV, and 15 kV. The composition of the samples and their corresponding forms were directly analyzed using an Oxford Ultim Max 65 energy dispersive spectrometer at a working distance of 15 μm (rated voltage and current of 15 kV and 15 mA, respectively). TEM characterization was performed using a JEOL JEM-ARM300F with an electron gun type of (FEG)/LaB_6, a point resolution of 0.19 nm and a line resolution of 0.10 nm at an operating acceleration voltage of 300 kV. Brunauer–Emmett–Teller (BET) surface adsorption tests were carried out using the fully automated physicochemical analyzer ASAP 2020 and MicroActive 5.02 system under the operating environment of Micromeritics® at 77 K and 87 K, with pore size statistics determined *via* the Barrett–Joyner–Halenda method. Using a PerkinElmer TGA 8000 thermogravimetric analyzer to perform thermogravimetric treatment on the mass of the samples, each sample was subjected to temperature rise testing within 12 hours at 60 °C under vacuum conditions.

Simulation section

Simulation parameters and conditions. Simulation parameters and conditionsThe basic structures of the original UIO-66 and MOF-74 mentioned in this article were introduced from the Cambridge Crystal Database (CCDC), and each referred to the unit cell parameters and working conditions of the basic framework structure. For the adsorption of hydrogen gas, the Reax Force Field series potential and OPLS-AA force field based on the LAMMPS software package under non-adiabatic equilibrium conditions were adopted. We introduced long-range interaction relationships and improved London dispersion for benchmark comparison. Additionally, the interactions between molecules and within molecules were tuned in order using Coulomb and van der Waals interactions. Specifically, to describe the electrostatic interactions between particles, the Ewald method was used to strengthen the role of electric charges. For specific description of the role of hydrogen molecules in the framework structure in this article from a clearer perspective, the Lorenz–Berthelot mixing criterion was employed to describe different bond-to-bond relationships. Subsequently, a Lennard–Jones (LJ) potential was applied for homogenization and coarsening treatment. At the same time, the position centers of hydrogen atoms and open metal atoms were introduced in different LJ settings with an expression and verification of override style. The simulation process of gaseous molecules underwent a thermal equilibrium relaxation of up to 150 ps within the temperature range of 0 K to 1000 K, and the hydrogen bond setting was constrained and controlled using the LINCS algorithm to achieve a thermal equilibrium temperature suitable for the system environment of the framework structure. The Berendsen barostat constant pressure relationship and the Parrinello–Rahman barostat constant pressure relationship were utilized to cope with the system pressure maintained for product generation and program operation within 100 bar (the compression rate was set to 5.0×10^{-5} bar^{-1}), accompanied by the Nosé–Hover thermostat constant temperature relationship with a coupling constant of 0.5 ps. Using the truncation mechanism under the Verlet algorithm, the phase radius was kept at the default value of 1.5 Å.

Conflicts of interest

There are no conflicts to declare.

Data availability

All data supporting the findings of this study are available within the article and its supplementary information (SI) files. Supplementary information: TEM and selected area electron diffraction (SAED), BET and pore distribution, simulation diagram of gas distribution, hydrogen adsorption, calculation of intermediate transition states for BDC, BPDC and TPDC, comparison of hydrogen uptake capacity and explanation on the calculation of statistical entropy. See DOI: **https://doi.org/10.1039/d5ra06111c**.

Acknowledgements

Thanks to the referee who provided suggestions, assistance, and support for this work.

References

1 IEA Hydropower, Flexible Hydropower Providing Value to Renewable Energy Integration, *IEA Hydrpower Annex IX// White Paper No.1*, 2019.
2 B. Evans and T. E. White, Argon Sorption at 77.4K on a Microporous Glass, *Nature*, 1968, **217**, 881–882.
3 O. M. Yaghi, G. M. Li and H. L. Li, Selective Binding and Removal of Guests in a Microporous Metal-Organic Framework, *Nat. Energy*, 1995, **378**, 703–706.
4 J. Brandt, T. Iversen, C. Eckert, F. Peterssen, B. Bensmann, A. Bensmann, M. Beer, H. Weyer and R. Hanke-Rauschenbach, Cost and Competitiveness of Green Hydrogen and the Effects of the European Union Regulation of Framework, *Nat. Energy*, 2024, **9**, 703–713.
5 J. F. Xing, L. Schweighauser, S. Okada, K. Harano and E. Nakamura, Atomistic Structures and Dynamics of Prenucleation Clusters in MOF-2 and MOF-5 Syntheses, *Nat. Commun.*, 2019, **10**, 3608.
6 K. Suresh, D. Aulakh, J. Purewal, D. J. Siegel, M. Veenstra and A. J. Matzger, Optimizing Hydrogen Storage in MOFs through Engineering of Crystal Morphology and Control of Crystal Size, *J. Am. Chem. Soc.*, 2021, **143**, 10727–10734.
7 O. C. Kwon, M. S. Kim, E. J. Choi, J. H. Bae, S. M. Yoo, J. C. Won, Y. H. Kim, J. H. Shin, J. S. Lee and D. W. Kim, High-aspect Ratio Zeolitic Imidazolate Framework (ZIF) Nanoplates for Hydrocarbon Separation Membranes, *Sci. Adv.*, 2022, **8**(1), eabl6841.
8 C. O. Ania, E. García-Pérez, M. Haro, J. J. Gutiérrez-Sevillano, T. Valdés-Solís, J. B. Parra and S. Calero, Understanding Gas-Induced Structural Deformation of ZIF-8, *J. Phys. Chem. Lett.*, 2012, **3**(9), 1159–1164.
9 Y. Y. Mao, J. W. Li, W. Cao, Y. L. Ying, P. Hu, Y. Liu, L. W. Sun, H. T. Wang, C. H. Jin and X. S. Peng, General Incorporation of Diverse Components Inside Metal-Organic Framework Thin Films at Room Temperature, *Nat. Commun.*, 2014, **5**, 5532.
10 S. M. Han, R. A. Ciufo, B. R. Wygant, B. K. Keitz and C. B. Mullins, Methanol Oxidation Catalyzed by Copper Nanoclusters Incorporated in Vacuum-Deposited HKUST-1 Thin Films, *ACS Catal.*, 2020, **10**(9), 4997–5007.
11 S. A. Mohamed, S. Y. Chong and J. H. Kim, Thermal Stability of Methyl-Functionalized MOF-5, *J. Phys. Chem. C*, 2019, **123**(49), 29686–29692.
12 A. M. Ebrahim, A. M. Plonka, N. Rui, S. Y. Hwang, W. O. Gordon, A. Balboa, S. D. Senanayake and A. I. Frenke, Capture and Decomposition of the Nerve Agent Simulant, DMCP, Using the Zeolitic Imidazolate Framework (ZIF-8), *ACS Appl. Mater. Interfaces*, 2020, **12**(52), 58326–58338.
13 M. Todaro, G. Buscarino, L. Sciortino, A. Alessi, F. Messina, M. Taddei, M. Ranocchiari, M. Cannas and F. M. Gelardi, Decomposition Process of Carboxylate MOF HKUST-1 Unveiled at the Atomic Scale Level, *J. Phys. Chem. C*, 2016, **120**(23), 12879–12889.
14 G. C. Lisensky and O. M. Yaghi, Visualizing Pore Packing and Topology in MOFs, *J. Chem. Educ.*, 2022, **99**(5), 1998–2004.
15 A. Banu, D. Friedrich, S. Brandani and T. Düren, A Multiscale Study of MOFs as Adsorbents in H_2 PSA Purification, *I&EC Res.*, 2013, **52**(29), 9946–9957.
16 W. Q. Gao, P. Cao, B. H. Li, L. Zhao, W. Z. Sun and W. Zhou, Unraveling the Role of Chemistry and Topology of MOFs in Psoralen Adsorption, *I&EC Res.*, 2022, **61**(20), 7172–7182.
17 R. A. Alabdulhadi, S. Khan, A. Khan, L. T. Alfuhaid, M. Y. Khan, M. Usman, N. Maity and A. Helal, Potential Use of Reticular Materials (MOFs, ZIFs, and COFs) for Hydrogen Storage, *ACS Appl. Energy Mater.*, 2025, **8**(3), 1397–1413.
18 K. H. Liu, Z. J. Chen, T. Islamoglu, S. J. Lee, H. Y. Chen, T. Yildirim, O. K. Farha and R. Q. Snurr, Exploring the Chemical Space of Metal-Organic Frameworks with rht Topology for High Capacity Hydrogen Storage, *J. Phys. Chem. C*, 2024, **128**(18), 7435–7446.
19 A. W. Thornton, C. M. Simon, J. H. Kim, O. Kwon, K. S. Deeg, K. Konstas, S. J. Pas, M. R. Hill, D. A. Winkler, M. Haranczyk, B. Smit and B. Materials, Genome in Action: Identifying the Performance Limits of Physical Hydrogen Storage, *Chem. Mater.*, 2017, **29**(7), 2844–2854.
20 S. M. Li, L. M. Zhang, P. W. Ye, M. Y. Zhu, Y. J. Nie, Y. W. Dai and F. Yang, Construction of Battery-Like Hierarchical MOF@MXene Heterostructures for Hybrid Supercapacitors, *Cryst. Growth Des.*, 2024, **24**(18), 7445–7454.
21 B. L. Suh and J. H. Kim, Ligand Insertion in MOF-74 as Effective Design for Oxidation of Ethane to Ethanol, *J. Phys. Chem. C*, 2018, **122**(40), 23078–23083.
22 Y. R. Jiang, X. Y. Hou, Y. Zhou, B. Y. Wang, T. S. Wang, L. P. Zhao, J. B. Wei, P. Sun and G. Y. Lu, Mapping the Nexus of Electrical Conductivity and Gas Sensing for Tailored Design of Transition Metal (Cu, Co, Ni)-Based Bimetallic 2D Conjugated MOF, *ACS Mater. Lett.*, 2025, **7**(1), 76–84.
23 S. G. Chong, S. M. J. Rogge and J. H. Kim, Tunable Electrical Conductivity of Flexible Metal-Organic Frameworks, *Chem. Mater.*, 2022, **34**(1), 254–265.
24 X. Q. Peng, J. Zhang, J. Q. Sun, X. C. Liu, X. F. Zhao, S. M. Yu, Z. P. Yuan, S. J. Liu and X. B. Yi, Hierarchically Porous Mg-MOF-74/Sodium Alginate Composite Aerogel for CO2 Capture, *ACS Appl. Nano Mater.*, 2023, **6**(18), 16694–16701.
25 Y. F. Zhang, C. M. Han, C. Bai, J. J. Ma, L. Yu, L. J. Sun, X. Y. Zhang and H. M. Hu, Supercapacitors Based on Mixed Nickel/Cobalt 2D MOF Coordination Nanosheets for Energy Storage, *ACS Appl. Nano Mater.*, 2024, **7**, 3897–3906.
26 B. Gibbons, E. M. Johnson, M. K. Javed, X. Z. Yang and A. J. Morris, Macromorphological Control of Zr-Based Metal-Organic Frameworks for Hydrolysis of a Nerve Agent Simulant, *ACS Appl. Mater. Interfaces*, 2024, **16**, 52703–52711.
27 H. Xia, N. Li, W. Q. Huang, Y. Song and Y. B. Jiang, Enzymatic Cascade Reactions Mediated by Highly Efficient Biomimetic Quasi Metal-Organic Frameworks, *ACS Appl. Mater. Interfaces*, 2021, **13**(19), 22240–22253.

28 H. Dong, L. H. Li, Z. D. Feng, Q. N. Wang, P. Luan, J. Li and C. Li, Amine-Functionalized Quasi-MOF for Direct Air Capture of CO_2, *ACS Mater. Lett.*, 2023, **5**(10), 2656–2664.

29 N. Y. Huang, B. X. Chu, D. Chen, B. Shao, Y. T. Zheng, L. Li, X. Xiao and Q. Xu, Rational Design of a Quasi-Metal-Organic Framework by Ligand Engineering for Efficient Biomass Upgrading, *J. Am. Chem. Soc.*, 2025, **147**(10), 8832–8840.

30 M. Bagheri, A. Melillo, B. Ferrer, M. Y. Masoomi and H. Garcia, Quasi-HKUST Prepared *via* Postsynthetic Defect Engineering for Highly Improved Catalytic Conversion of 4-Nitrophenol, *ACS Appl. Mater. Interfaces*, 2022, **14**(1), 978–989.

31 J. Jiang, W. Wei, Y. Tang, S. Y. Yang, X. Z. Wang, Y. Xu and L. H. Ai, In Situ Implantation of Bi2S3 Nanorods into Porous Quasi-Bi-MOF Architectures: Enabling Synergistic Dissociation of Borohydride for an Efficient and Fast Catalytic Reduction of 4-Nitrophenol, *Inorg. Chem.*, 2022, **61**(49), 19847–19856.

32 H. L. Qu, K. L. Liu, Q. L. Li, T. T. Cao, G. Chen, H. T. Guan, C. J. Dong and Z. Y. Yin, MOF-on-MOF Derived Co_2P/Ni_2P Heterostructures for High-Performance Supercapacitors, *J. Phys. Chem. Lett.*, 2024, **15**(40), 10181–10189.

33 Y. W. Foong, M. S. Hossain, S. V. Sukhomlinov, K. H. Bevan and T. J. Kemp, Faradaic Quantized Capacitance as an Ideal Pseudocapacitive Mechanism, *J. Phys. Chem. C*, 2021, **125**(8), 4343–4354.

34 G. Dai, Y. Li, Z. Li, J. W. Zhang, X. Geng, F. Zhang, Q. J. Wang and P. G. He, Zirconium-Based Metal-Organic Framework and $Ti_3C_2T_x$ Nanosheet-Based Faraday Cage-Type Electrochemical Aptasensor for Escherichia coli Detection, *ACS Appl. Nano Mater.*, 2022, **5**(7), 9201–9208.

35 S. Kampouri, F. M. Ebrahim, M. Fumanal, M. Nord, P. A. Schouwink, R. Elzein, R. Addou, G. S. Herman, B. Smit, C. P. Ireland and K. C. Stylianou, Enhanced Visible-Light-Driven Hydrogen Production through MOF/MOF Heterojunctions, *ACS Appl. Mater. Interfaces*, 2020, **13**(12), 14239–14247.

36 J. M. Yu, L. H. Xie, J. R. Li, Y. G. Ma, J. M. Seminario and P. B. Balbuena, CO_2 Capture and Separations Using MOFs: Computational and Experimental Studies, *Chem. Rev.*, 2017, **117**(14), 9674–9754.

37 M. A. Syzgantseva and O. A. Syzgantseva, Efficient Computation of Nonadiabatic Coupling Coefficients for Modeling Charge Carrier Recombination in Extended Systems: The Case of Metal-Organic Frameworks, *J. Phys. Chem. A*, 2021, **125**(44), 9700–9706.

38 R. V. Listyarini, J. Gamper and T. S. Hofer, Storage and Diffusion of Carbon Dioxide in the Metal Organic Framework MOF-5—A Semi-empirical Molecular Dynamics Study, *J. Phys. Chem. B*, 2023, **127**, 9378–9938.

39 H. Mashhadimoslem, M. A. Abdol, P. Karimi, K. Zanganeh, A. Shafeen, A. Elkamel and M. Kamkar, Computational and Machine Learning Methods for CO_2 Capture Using Metal-Organic Frameworks, *ACS Nano*, 2024, **18**(35), 23842–23875.

40 S. P. Veccham and M. Head-Gordon, M. Assessment of Performance of Density Functionals for Predicting Potential Energy Curves in Hydrogen Storage Applications, *J. Phys. Chem. A*, 2021, **125**(19), 4245–4257.

41 A. von Wedelstedt, G. Goebel and G. Kalies, MOF-VR: A Virtual Reality Program for Performing and Visualizing Immersive Molecular Dynamics Simulations of Guest Molecules in Metal-Organic Frameworks, *J. Chem. Inf. Model.*, 2022, **62**(5), 1154–1159.

42 B. Q. Sun, T. Y. Tao, L. Liu, R. Ding and Y. Y. Mao, Electron Transfer Facilitated by π–π Stacking during the Nitrobenzene Recognition Process of an MOF Sensor, *J. Phys. Chem. C*, 2021, **125**(22), 12433–12440.

43 D. K. Chandra, A. Kumar and C. Mahapatra, High-Precision Multistage Molecular Dynamics Simulations and Quantum Mechanics Investigation of Adsorption Mechanisms of Cerium-Based H_3BTC MOF (Ce-H_3BTC-MOF) on Pristine and Functionalized Carbon Nanotubes, *Langmuir*, 2025, **41**(23), 14889–14914.

44 B. Singh, T. Kim, Y. Hassan, M. Joe, K. Watanabe, T. Taniguchi, W. J. Yoo, P. K. Srivastava and C. Lee, Topology-Driven Coulomb Drag in van der Waals Heterostructure with Broken Inversion Symmetry, *ACS Appl. Mater. Interfaces*, 2024, **16**(24), 31247–31253.

45 I. Park and B. G. Jang, Nonlocal Coulomb Interaction in Mixed-Valence Material $LiCu_2O_2$, *Nano Lett.*, 2025, **25**(26), 10442–10448.

46 H. Rothery, *Electrons, Atoms, Metals and Alloys*, Philosophical Library, New York, 1955, 2, 387.

47 Z. Ji, T. Li and O. M. Yaghi, Sequencing of Metals in Multivariate Metal-Organic Frameworks, *Science*, 2020, **369**(6504), 674–680.

48 X. Xu, Z. H. Chen and Y. Yang, Molecular Dynamics with Constrained Nuclear Electronic Orbital Density Functional Theory: Accurate Vibrational Spectra from Efficient Incorporation of Nuclear Quantum Effects, *J. Am. Chem. Soc.*, 2022, **144**(9), 4039–4046.

49 T. Matsuda, O. Kamimura, H. Kasai, K. Harada, T. Yoshida, T. Akashi, A. Tonoruma, Y. Nakayama, J. Shimoyama, K. Kishio, T. Hanaguri and K. Kitazawa, Oscillating Rows of Vortices in Superconductors, *Science*, 2001, **294**(5549), 2136–2138.

50 Y. Lu, Y. R. Xing, J. W. Tao, S. Wang, G. Y. Lin, H. T. Zhang and H. B. Qiu, A Highly Sensitive Piezoresistive Electronic Skin: Coulomb Blockade-Favored Dynamic Conduction Paths in Micellar Brush-Templated Metal Nanoarrays, *Chem. Mater.*, 2025, **37**(9), 3274–3283.

51 Y. B. N. Tran, P. T. K. Nguyen, Q. T. Luong and K. D. Nguyen, Series of M-MOF-184 (M = Mg, Co, Ni, Zn, Cu, Fe) Metal-Organic Frameworks for Catalysis Cycloaddition of CO_2, *Inorg. Chem.*, 2020, **59**(22), 16747–16759.

52 S. Park, J. H. Lee, B. K. Kim, C. Y. Jung, S. E. Bae, J. G. Kang, D. H. Moon and J. H. Park, Radical-Driven Crystal-Amorphous-Crystal Transition of a Metal-Organic Framework, *J. Am. Chem. Soc.*, 2024, **146**(13), 9293–9301.

53 T. Stolar, A. Prašnikar, V. Martinez, B. Karadeniz, A. Bjelić, G. Mali, T. Friščić, B. Likozar and K. Užarević, Scalable Mechanochemical Amorphization of Bimetallic Cu-Zn MOF-74 Catalyst for Selective CO_2 Reduction Reaction to

Methanol, *ACS Appl. Mater. Interfaces*, 2021, **13**(2), 3070–3077.

54 P. Das and A. Chattopadhyay, Enhanced Chemical Stability in the Twisted Dodecagonal Stacking of Two-Dimensional Copper Nanocluster Assemblies, *J. Phys. Chem. Lett.*, 2022, **13**(37), 8793–8800.

55 K. M. ElSawy, R. Twarock, D. P. Lane, C. S. Verma and L. S. D. Caves, Characterization of the Ligand Receptor Encounter Complex and Its Potential for *in Silico* Kinetics-Based Drug Development, *J. Chem. Theory Comput.*, 2012, **8**(1), 314–321.

56 J. Ge, X. Cheng, L. H. Rong, J. R. Capadona, E. B. Caldona and R. C. Advincula, 3D Temperature-Controlled Interchangeable Pattern for Size-Selective Nanoparticle Capture, *ACS Appl. Mater. Interfaces*, 2024, **16**(10), 12232–12243.

57 L. Z. Xu, X. Z. Wang, Y. Kim, T. C. Shyu, J. Lyu and N. A. Kotov, Kirigami Nanocomposites as Wide-Angle Diffraction Gratings, *ACS Nano*, 2016, **10**(6), 6156–6162.

58 S. E. Henkelis, D. Rademacher, D. J. Vogel, N. R. Valdez, M. A. Rodriguez, L. E. S. Rohwer and T. M. Nenoff, Luminescent Properties of DOBDC Containing MOFs: The Role of Free Hydroxyls, *ACS Appl. Mater. Interfaces*, 2020, **12**(20), 22845–22852.

59 A. Kultaeva, A. Pöppl and T. Biktagirov, Atomic-Scale Quantum Sensing of Ensembles of Guest Molecules in a Metal-Organic Framework with Intrinsic Electron Spin Centers, *J. Phys. Chem. Lett.*, 2022, **13**(29), 6737–6742.

60 Z. X. Cai, Y. J. Xia, Y. Ito, M. Ohtani, H. Sakamoto, A. Ito, Y. J. Bai, Z. L. Wang, Y. Yamauchi and T. Fujita, General Synthesis of MOF Nanotubes *via* Hydrogen-Bonded Organic Frameworks toward Efficient Hydrogen Evolution Electrocatalysts, *ACS Nano*, 2022, **16**(12), 20851–20864.

61 B. M. Raffah, H. Hassan, M. W. Iqbal and Y. Al-Hadeethi, Synergistic Co-MOF/ZnS Composite: Advancing Supercapattery Performance and Catalyzing Hydrogen Evolution Reaction, *Energy Fuels*, 2024, **38**(4), 3477–3490.

62 A. Q. Liu, X. Peng, Q. B. Jin, S. K. Jain, J. M. Vicent-Luna, S. Calero and D. F. Zhao, Adsorption and Diffusion of Benzene in Mg-MOF-74 with Open Metal Sites, *ACS Appl. Mater. Interfaces*, 2019, **11**(4), 4686–4700.

63 K. F. Wang, Y. J. Chen, R. Tian, H. Li, Y. Zhou, H. Duan and H. Z. Liu, Porous Co-C Core-Shell Nanocomposites Derived from Co-MOF-74 with Enhanced Electromagnetic Wave Absorption Performance, *ACS Appl. Mater. Interfaces*, 2018, **10**(13), 11333–11342.

64 P. I. Scheurle, A. Mähringer, T. Haug, A. Biewald, D. Axthammer, A. Hartschuh, L. Harms, G. Wittstock, D. D. Medina and T. Bein, Helical Anthracene-Ethyne-Based MOF-74 Analogue, *Cryst. Growth Des.*, 2022, **22**(5), 2849–2853.

65 C. Wang, L. J. Li, S. F. Tang and X. B. Zhao, Enhanced Uptake and Selectivity of CO2 Adsorption in a Hydrostable Metal-Organic Frameworks *via* Incorporating Methylol and Methyl Groups, *ACS Appl. Mater. Interfaces*, 2014, **6**, 16932–16940.

66 K. S. Song, D. Kim, A. Coskun and A. Hierarchically, Porous Reduced Graphene Oxide Coated with Metal-Organic Framework HKUST-1 for Enhanced Hydrogen Gas Affinity, *ACS Appl. Nano Mater.*, 2020, **3**(2), 985–991.

67 T. Pham, K. A. Forrest, K. J. Chen, A. Kumar, M. J. Zaworotko and B. Space, Theoretical Investigations of CO_2 and H_2 Sorption in Robust Molecular Porous Materials, *Langmuir*, 2016, **32**(44), 11492–11505.

68 D. A. Gómez-Gualdrón, T. C. Wang, P. García-Holley, R. M. Sawelewa, E. Argueta, R. Q. Snurr, J. T. Hupp, T. Yildirim and O. K. Farha, Understanding Volumetric and Gravimetric Hydrogen Adsorption Trade-off in Metal-Organic Frameworks, *ACS Appl. Mater. Interfaces*, 2017, **9**(39), 33419–33428.